https://doi.org/10.5194/egusphere-2026-1393
Preprint. Discussion started: 14 April 2026

Nascent Eocene Indian Monsoons recorded in oyster shells from the western Indian margin

Aniket Mitra[1,2], Steven Goderis[2], Niels J. de Winter[2,3], Michiel Baatsen[4], Béatrice A. Ledésert[1], Guillaume Dupont-Nivet[5,6], Philippe Claeys[2,7], Inigo A. Müller[2]

[1]Institut des Sciences de la Terre de Paris (ISTeP), CY Cergy Paris Université, 95000 Neuville-sur-Oise, France

[2]Archaeology, Environmental Changes and Geo-Chemistry (AMGC), Vrije Universiteit Brussel, 1050 Brussels, Belgium

[3]Department of Earth Sciences, Vrije Universiteit Amsterdam, Amsterdam, the Netherlands

[4]Institute for Marine and Atmospheric Research Utrecht, Utrecht University, Utrecht, The Netherlands

[5]Géosciences Rennes, CNRS-University of Rennes, Rennes, France

[6]Helmholz Center, GeoForschungZentrum (GFZ), Potsdam, Germany

[7]Department of Earth, Ocean and Atmospheric Sciences, University of British Columbia, Vancouver, BC V6T 1Z4, Canada

Correspondence to: Aniket Mitra (amiaranya8@gmail.com)

Abstract. The origin, intensification and paleogeographic drivers of the South Asian Monsoon (SAM) since the Eocene, remain poorly understood mainly due to the paucity of suitable seasonal proxies coupled with climate simulations. This study evaluates the seasonal climate variability and potential presence of SAM-like conditions based on geochemical proxy-based sub-annual climatic reconstruction recovered from late-middle Eocene fossil oyster shell material from the Kutch basin (India), interpreted in the framework of Community Earth System Model (CESM) climate simulations. A thick-shelled honeycomb oyster species *Pycnodonte kachchhensis* is used as a natural palaeoclimate archive. Bulk sediment organic carbon isotope stratigraphy places the oyster horizon within the late Bartonian, after the Middle Eocene Climatic Optimum (MECO) from which a previous oyster fossil study provides comparison. Clumped isotope thermometry indicates low seasonal variability with sea surface temperatures of $31^{+2.2}_{-2.1}$ to $36^{+2.8}_{-2.7}$ °C and evaporative conditions ($\delta^{18}O_w$: $0.6^{+0.4}_{-0.4}$ to $1.6^{+0.6}_{-0.5}$ ‰), within a restricted late Bartonian lagoonal setting. Trace element profiles in oyster shells indicate a low-nutrient environment and capture around two years of the oysters' lifespan, reflected in seasonal variations along the shell growth axis. Stable isotope data from the multiyear shell archive indicates annual temperature drops associated with periods of higher rainfall to evaporation. The observed pattern is consistent with CESM simulation showing a nascent SAM as well as precipitation outside the main monsoon months due to moisture transport from the open seaway between India and Eurasia. However, a modern-like monsoon with strong seasonal contrasts and pronounced winter temperature minima was not yet established in the study area, possibly owing to the tropical palaeolatitude of the region (~8° N) and palaeogeographic factors such as the open northern seaway of Greater India. Observed climatic and seasonal variability are comparable to the underlying MECO oyster record, despite the early Bartonian hyperthermal conditions and the gradual decline in pCO_2 toward the late Bartonian, suggesting a limited sensitivity of equatorial climate to atmospheric CO_2.

1 Introduction

Significant tectonic and palaeogeographic changes in Asia involving the collision of the Indian subcontinent with Eurasia, the closure of the Himalayan Foreland Basin, the retreat of the Central Asian Paratethys, and the uplift of the Tibetan Plateau since the middle Eocene are designated as potential drivers of the onset, intensification and modulation of the South Asian Monsoon (SAM) until its modern establishment (Huber and Goldner, 2012; Dimri et al., 2016; Tardif et al., 2020, 2023; Mitra and Halder, 2024). However, deciphering between these potential drivers is difficult because the timing of the onset and intensification of the SAM remains debated, with estimates ranging from the late Eocene (~40 Ma) to the early Miocene (~20 Ma), based on both climate modelling and proxy-based studies (Abhik et al., 2026 and references therein). While some researchers propose that a fully developed SAM existed by the late Eocene (Huber and Goldner, 2012; Licht et al., 2014), others argue that a modern-like Indian monsoon system, characterized by strong summer precipitation had not yet fully formed during that time (Tada et al., 2016). Rather an arid zone is suggested for Northern India from 42-38 Ma by climate modelling with seasonal changes associated with shifts of the Intertropical Convergence Zone (ITCZ) towards low latitude equatorial regions (Tardif et al., 2020, 2023).

Proxy records of monsoonal conditions are challenging because typical palaeoclimate proxies record long-term climate trends over thousands to millions of years rather than shorter-term climate variability, down to the seasonal scale, required to detect monsoons. Calcium carbonate shells of molluscs, which grow incrementally, capture climatic and environmental signals throughout their ontogeny at a sub-annual to seasonal and even day scale resolution (Stenzel, 1971; Kirby et al., 1998; Evans et al., 2013; Bougeois et al., 2016; de Winter et al., 2017a, 2020; Scholz et al., 2024). Stable isotope sclerochemistry of fossil shells is a powerful tool for reconstructing sub-annual climate, as growth-increment-resolved carbonate records capture changes in temperature, and hydrologic cycle (de Winter et al., 2018; Arndt et al., 2025; Mitra et al., 2025). Oyster shell exhibit cyclical, seasonal patterns in stable isotopes, as well as in trace element to calcium concentration ratios (Mg/Ca, Sr/Ca, Cu/Ca, Zn/Ca, Ba/Ca etc.; Mouchi et al., 2013, 2025; Bougeois et al., 2014, 2016; de Winter et al., 2018, 2020, 2021; Mitra et al., 2025). The incorporation of certain trace elements in bivalve shells has been interpreted to vary with seasonality and environmental conditions (Goodwin et al., 2013; Burioli et al., 2017; Poitevin et al., 2020; Liu et al., 2021; Budko et al., 2021; Mamede et al., 2022; Cardoso da Silva et al., 2024). The geochemical behaviour of rare earth elements (REE) investigated in fossil oyster shells suggest that REE signatures can be preserved and potentially reflect paleoenvironmental conditions, but these patterns can be affected by diagenetic overprints and biological fractionation (Akagi and Edanami, 2017; Briant et al., 2021; Valdés-Vilchis et al., 2021; Mouchi et al., 2020; Barrat et al., 2023); for example, REE patterns in *Crassostrea gigas* reflect environmental variations, while REE incorporation in *Ostrea edulis* appears largely unaffected by environmental factors (Mouchi et al., 2020). Based on a careful assessment of the integration of trace element, REE concentrations and stable isotope geochemistry from fossil oysters, this study explores the seasonal variability and environmental control on these proxies while attempting to reconstruct seasonal variations related to SAM in the ideally located late middle Eocene Kutch Basin, western India.

The pericratonic Kutch Basin belongs to the circum-Tethyan carbonate ramp that evolved in response to the Eocene tectonic reorganization associated with the India-Asia collision (Mutti and Hallock, 2003; Höntzsch et al., 2011; Martín-Martín et al., 2024). The easternmost extension of the carbonate ramp, represented by a very thick limestone deposition (the Fulra Limestone), formed in the late Bartonian tropics (Biswas, 1992; van Hinsbergen et al., 2015; Banerjee et al., 2018; Fig. 1a-d). This formation postdates the Middle Eocene Climatic Optimum (MECO ~41 Ma; Khanolkar et al., 2017) characterized by high temperatures of 32-35 °C (Mitra et al., 2025), and predates the late Oligocene cooling (Sarkar et al., 2003). Though, records from the early to middle Eocene preceding the carbonate ramp formation (Mitra et al., 2022, 2025; Evans et al., 2018) are available, climatic conditions and seasonal dynamics during the ramp formation itself remain unrecorded in Kutch, despite its particularly strong potential to provide a seasonal record to test the alleged occurrence of monsoons in that period as well as quantify its intensity and determine its characteristics.

The Fulra Limestone is characterized by an abundance of Larger Benthic Foraminifera (LBF; Fig. 1d-j), with molluscan assemblages dominated by two exceptionally large species, the oyster *Pycnodonte kachchhensis* Kachhara et al., 2011 and the gastropod *Turbinella bulbiformis* Sowerby, 1840, both originating from the lower part of the formation (Fig. 1d, g-h; Kachhara et al., 2011). The thick-shelled oyster *P. kachchhensis*, with its preserved calcium carbonate shell, is used in this study as a palaeoclimate archive. *Pycnodonte* Fischer Von Waldheim, 1835, (family Gryphaeidae Vialov, 1936), an extinct sessile oyster genus, incorporate continuous area-specific information into their shells, especially in the resistant foliated calcite layers, making them excellent archives for palaeoclimate and palaeoenvironmental reconstructions (de Winter et al., 2018). They are predominantly found in palaeotropical regions but also occur in higher latitudes, highlighting their adaptability to a broad range of conditions from stable offshore settings to shallower, waterlogged substrates (Bottjer et al., 1978; Dhondt et al., 1984; de Winter et al., 2018). We present here climate proxy results from these ideal fossil targets. We first assessed the stratigraphic position of the studied oyster species in relation to global warming and cooling events using stable carbon isotope ($\delta^{13}C_{org}$) chemostratigraphy from bulk sediment samples of the Bartonian Kutch. Seasonally resolved temperatures were then estimated through clumped isotope (Δ_{47}) thermometry from the calcitic shell of the oyster species. The $\delta^{18}O_w$ of the water inhabited by the oysters, which is influenced by the precipitation-evaporation cycle and surrounding environmental factors, was estimated from the combination of clumped and oxygen isotope values (see e.g. Caldarescu et al., 2021). Proxy-based reconstructions of sub-annual temperature and hydrological variability were compared with Community Earth System Model (CESM) simulations (Baatsen et al., 2020), yielding insights into seasonality and monsoon dynamics during this critical period.

2 Geological settings

The studied successions of the Kutch (or Kachchh) Basin comprise the Harudi Formation and the Fulra Limestone (Biswas, 1992; Fig. 1d). These formations were assigned a late-middle Eocene (Bartonian) age primarily based on Larger Benthic Foraminifera (LBF), and broadly supported by dinoflagellate assemblage, smaller benthic and planktic foraminifera, and strontium isotope ratios (Fig. 1d, Anwar et al., 2013; Saraswati et al., 2016, 2018; Khanolkar and Saraswati, 2015, 2019; Das et al., 2024). We report here chemostratigraphic data from these Harudi Formation and Fulra Limestones and schlerochemistry results from oyster fossils recovered from the Fulra Limestone that complement previous results from fossil oysters from the Harudi Formation (Mitra et al., 2025).

The Fulra Limestone, characterized by a carbonate platform deposition (Shallow Benthic Zone: SBZ17; Planktic Foraminiferal Zone E12; Fig. 1d; Khanolkar and Saraswati, 2019), is part of the Eocene circum-Tethys carbonate ramp system (Racey, 2001; Banerjee et al., 2018). It was deposited in environments ranging from shallow lagoons to deeper open marine settings, as evidenced by orthophragminid mudstone, nummulitic grainstone, and *Alveolina* wackestone (Fig. 1d-j; Banerjee et al., 2018). *P. kachchhensis* specimens for this study are sampled from the lower part of the Fulra Limestone, ~5-7 meters above the Harudi-Fulra boundary and coinciding with the first appearance of LBF species *Alveolina elliptica* (Fig. 1d,g-h; SBZ17, E12: Banerjee et al., 2018). The oyster specimens occur within limestone matrix (Fig. 1d,g). We sampled oyster shells preserved within the rock that are generally intact, closely packed, and in some cases articulated and preserved in life position. Loose shells affected by apparent weathering of the limestone commonly were discarded. The depositional unit containing *Alveolina* wackestone, indicates a lagoonal setting bordered by nummulitic grainstone (Banerjee et al., 2018; Das et al., 2024). Further stratigraphic age and depositional environment interpretations will be discussed in light of the results.

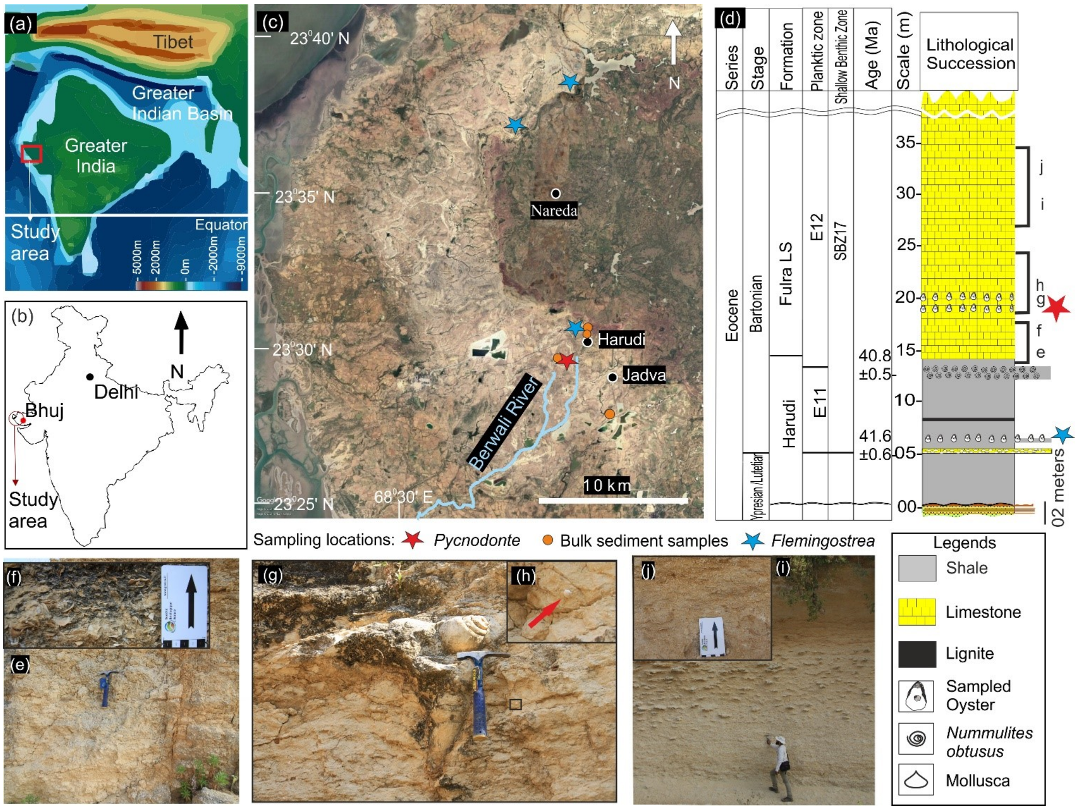

Figure 1. Palaeogeographic position of India during (a) Baronian with palaeo-altitude following Montheil et al., 2026; (b) Position of the study site in present Indian political map; (c) Satellite image of the study locality (Source: Images © 2025 NASA, Map data © 2025 Google - https://maps.google.com, last access: 16 January 2026) with sampling location of *Pycnodonte*, bulk sediment samples (this study), and *Flemingostrea* (Mitra et al., 2025). (d) Lithostratigraphic section of the Bartonian onshore Kutch Basin; biostratigraphy following Khanolkar and Saraswati (2015, 2019), Banerjee et al. (2018) and Das et al. (2024); (e-j) Fulra Limestone field photographs: (e-f) Basal Fulra Limestone vertical section with high concentration of *Discocyclina* sp. near Harudi Formation type section; (g-h) Fulra Limestone unit with *T. bulbiformis* and *P. kachchhensis*; (h) *Alveolina* sp. at the banks of Berwali River; (i) Top of Fulra Limestone unit with high concentration of (j) *Discocyclina* sp. near Jadva village.

3 Materials and methods

3.1 Bulk sediment samples δ^{13}C$_{org}$ measurement

A total of 46 sediment samples were systematically collected at 0.70 m stratigraphic intervals, with additional sampling at lithological contacts, from surface exposures extending from the Harudi Formation (early Bartonian) to the uppermost Fulra Limestone (late Bartonian) in the Kutch Basin (Fig. 1d-i). The Harudi Formation samples were collected from the Harudi type section (Fig. 1c-d; 23°31'33.58" N, 68°41'7.89" E). Fulra Limestone samples were collected from exposures near the Harudi village (Fig. 1c-d, e-f; 23°31'25.80" N, 68°41'7.94" E) and the banks of the Berwali river (Fig. 1c-d, g-h; 23°30'23.56" N, 68°40'2.51" E) for the lower part, and another vertical section (Fig. 1c-d, i-j; 23°30'32.80" N, 68°36'38.64" E) near the village of Jadva, containing its boundary with the overlying Maniyara Fort Formation (Oligocene). The sedimentary rock samples were weighed and treated with 2M hydrochloric acid and left for 24 hours to ensure complete inorganic carbon removal as CO_2. The remaining sample fractions were separated from the residual acid through repeated washing with deionized water. The samples were then oven dried at 60 °C.

The $\delta^{13}C_{org}$ was determined by a Euro EA Elemental Analyzer (CHNS) and EuroVector HT-PyrOH combustion system coupled to a Nu Instruments Horizon 2 isotope ratio mass spectrometer. The results are calibrated using two international standards, IAEA-C6 (sucrose $\delta^{13}C = -10.45$ ‰) and IA-R068 (soy protein $\delta^{13}C = -25.22$ ‰), together with in-house reference material IVA33802153 (organic-poor sediment $\delta^{13}C = -22.88$ ‰), which is calibrated against these international standards. All $\delta^{13}C_{org}$ values are reported relative to Vienna Peedee Belemnite (VPDB). Standard deviations for all standards based on repeated analyses are as follows: IAEA-C6 (sucrose): ±0.25 ‰ (n = 13), IA-R068 (soy protein): ±0.82 ‰ (n =13), and IVA33802153 (organic-poor soil): ±0.39 ‰ (n = 4). The $\delta^{13}C_{org}$ values were plotted against the lithostratigraphic column. Rapid environmental perturbations and depositional hiatuses can produce spurious shifts in $\delta^{13}C_{org}$ records; therefore, we have applied a three-point moving average to smooth out short-term noise and reveal systematic excursion(s) (Table S1).

3.2 Oyster sample preparation

Three very thick shelled *P. kachchhensis* specimens (Figs. 2, S1), collected from a surface exposure of Fulra Limestone near Harudi village (Fig. 1A-C; 23°30′23.56″N, 68°41′02.51″E), close to Berwali river during a fieldwork trip in January 2024 were selected for this study. The specimens were cleaned, dissected using a diamond coated saw, and one halves were prepared as 05 mm thick sections following the methodology outlined in Mitra et al. (2025). The other halves of the sections were prepared as thin sections by mounting on glass slides and polishing them to a final thickness of 100 µm. The thick sections were analyzed using micro-X-ray fluorescence (µ-XRF) and Laser Ablation - Inductively Coupled Plasma Mass Spectrometry (LA-ICP-MS), and finally micro-drilled to collect calcite powder for conventional oxygen ($\delta^{18}O_{cc}$), carbon ($\delta^{13}C_{cc}$) and clumped isotope (Δ_{47}) analyses, while the thin sections underwent microscopic colour scanning and scanning electron microscopy analyses.

3.3 Microscopy and scanning electron microscopy

The thin sections were photographed using an Olympus BX43 visible light microscope equipped with SC50 camera (ISTeP, CYU). Secondary electron images were acquired using a Zeiss GeminiSEM 300 at CYU Scanning Electron Microscope under high vacuum (HV) conditions, with a 60 µm aperture and an accelerating voltage (EHT) of 15 kV.

3.4 Micro-X-ray fluorescence

Elemental mapping of major and trace elements (e.g., Ca, Si, Fe, Mn) was performed using the Bruker M4 Tornado energy-dispersive µXRF scanner (Bruker Nano GmbH, Berlin, Germany) at AMGC-VUB. The mapping acquisition settings follow the methodologies outlined by de Winter and Claeys (2017) and Kaskes et al. (2021). High-resolution mapping of shell cross sections was conducted with an X-ray spot size of 25 µm and a dwell time of 10 milliseconds per spot. Given that Mn and Fe are primary indicators of diagenetic remineralization in calcite minerals (Al-Aasm and Veizer; 1986; Steuber, 1999; de Winter et al., 2018), shells displaying minimal Mn and Fe concentrations, especially in the resilifer region, were used for stable isotope analyses. Micro-X-ray fluorescence line scans were carried out on the most pristine resilifer-edges of the specimens using a

25 µm spot size with a 25 µm gap between spots, and a dwell time of 60 seconds per spot, following recommendations for optimal balance between spectral quality and spatial resolution (de Winter et al., 2017b). The line scanning setup ensured sufficient time to generate stable spectra with quantifiable results for elements of interest, in accordance with the recommendations of de Winter and Claeys (2017). All µ-XRF line scans were quantified using the Bruker Esprit fundamental parameters (FP) method, calibrated against the BAS CRM 393 limestone standard (Bureau of Analyzed Samples, Middlesbrough, UK).

3.5 Element concentration line scans from Laser Ablation-Inductively Coupled Plasma-Mass Spectrometry (LA-ICP-MS)

Spatially resolved elemental concentrations for Na, Mg, Ca, Ti, Mn, Fe, Ni, Cu, Zn, Sr, Ba, La, Ce, Pr, Nd, Sm, Pb, Th and U were calculated from a calibrated transient signal recorded during LA-ICP-MS line scanning in the growth direction on the thick sections of the *P. kachchhensis* shells (K/Pk/01,K/Pk/02 and K/Pk/03) and additionally three pristine *F. pseudoflemingi* shells of the early Bartonian Kutch (K/Fl/15, K/Fl/38, K/Fl/57; Mitra et al., 2025). Two parallel line-scans were conducted on each pycnodont shell: one along the resilifer edge, following the same path as the non-destructive µ-XRF scan, and the other approximately 2 mm further inside the cross-section. The analysis was carried out at the ICP-MS lab of AMGC-VUB relying on a Teledyne Iridia 500 Hz 193 nm ArF excimer laser system coupled to an Agilent Technologies 8900 configuration for Advanced Applications tandem ICP-MS instrument. Continuous scanning along shell transects using a laser spot of 25 µm and sampling interval of 25 µm yielded a total of 4812 datapoints. Elemental concentrations were calibrated by bracketing the analysis runs with certified reference materials from the US Geological Survey (USGS), including BIR-1G, BHVO-2G, and Max Planck Institute - DING Reference Glass standards GOR128-G, GOR132-G, StHs6/80-G, ML3B-G, ATHO-G, KL2-G, as well as Standard Reference Material SRM612 from the National Institute of Standards and Technology (NIST). Based on repeated analyses of these reference materials, accuracy and precision is estimated to be better than 5-15% relative standard deviation (RSD), depending on the determined concentration level.

3.6 Stable carbon ($\delta^{13}C_{cc}$) and oxygen ($\delta^{18}O_{cc}$) isotope analysis

Calcite powder samples were collected by drilling at regular intervals of 1 mm from the resilifers of two *P. kachchhensis* oyster specimens K/Pk/01 and K/Pk/02. The drilling was carried out by a computer-driven high precision Merchantek video controlled micro-mill device at AMGC-VUB laboratory using a tungsten drill-bit of 300 nm. The drilling speed was set to 5 %, and the drill bit was stopped every five seconds to prevent overheating and damage to the calcite crystals. The surface of the oysters and the drill bit were cleaned after every sample.

Aliquots of 250-300 µg of the sample powder were subjected to a reaction with 104 % phosphoric acid (H_3PO_4) at 70 °C in a NuCarb carbonate preparation device. The resulting stable oxygen and carbon isotope compositions ($\delta^{13}C_{cc}$ and $\delta^{18}O_{cc}$) were determined with a Nu-Perspective isotope ratio mass spectrometer at the AMGC-VUB lab. The $\delta^{13}C_{cc}$ and $\delta^{18}O_{cc}$ values reported in this study are expressed in per mil (‰) units relative to the VPDB standard. As reference material the calcitic NBS-19 ($\delta^{13}C$: 1.95 ‰; $\delta^{18}O$: -2.2 ‰) was used, while an in-house Marbella marble standard ($\delta^{13}C$: 3.41 ± 0.05 ‰; $\delta^{18}O$: 0.13 ± 0.10 ‰; n = 15) was measured after every seventh sample for drift correction and quality control.

3.7 Clumped isotope (Δ_{47}) thermometry

Clumped isotope thermometry was performed on equidistantly (1 mm) sampled calcite powders from the resilifer region of K/Pk/02, which shows clear quasi-cyclic pattern in its $\delta^{18}O_{cc}$ and trace elements to calcium profiles (see Sect. 5.1) and has evidence of minimum Mn and Fe incorporation. Aliquots of 4.5-5.5 mg were taken from each powdered sample, representing zones with relatively higher and lower $\delta^{18}O_{cc}$ values. Nine to 11 replicates of ~500 µg were analyzed of each drilled powder. The clumped isotope measurements were carried out using a NuCarb preparation device connected to a Perspective-IS isotope ratio mass spectrometer equipped with extra Faraday cups to record besides the more common CO_2 isotopologues (m/z 44 to 46) also the less abundant isotopologues with mass 47, 48 and 49 at AMGC-VUB. In each measurement sequence, a set of the calcitic ETH4, IAEA C1 and IAEA C2 standards was included as check standards to monitor the performance of the analytical setup and correction procedure. The $\Delta_{47\text{-raw}}$ data were processed with simultaneously measured ETH-1, ETH-2 and ETH-3 standards, from which an empirical transfer function (ETF) was determined by plotting their raw values versus their published accepted values at the I-CDES90 scale (Bernasconi et al., 2018; 2021). The ETF was constrained with the EASOTOPE software (John and Bowen, 2016) for the whole correction interval used for this project and then used to convert the $\Delta_{47\ \text{raw}}$ of unknown samples and check standards into the final $\Delta_{47\ \text{I-CDES90}}$ values. The temperature relationship of Anderson et al. (2021) was applied to derive the Δ_{47}-temperature as this calibration was constrained with the same set of calcite standards. Raw carbon and oxygen isotope values were converted relative to VPDB with a drift correction using the ETH-1, ETH-2 and ETH-3 standards with their published values of Bernasconi et al. (2018) and in case of the oxygen isotope composition, the acid fractionation of 1.00871 (Kim et al., 2007) was added prior to the drift correction. The relationship by Kim and O'Neil (1997) was used to calculate the oxygen isotope composition of the water source ($\delta^{18}O_w$) in which the shells formed from the paleotemperature and the $\delta^{18}O_{cc}$ value. Uncertainties of the clumped isotope analysis results are reported with 95% confidence intervals.

3.8 Data analysis

3.8.1 Trace element data processing and multivariate analysis

The raw dataset of trace elements from LA-ICP-MS was processed through background and drift correction and data normalization (Lin et al., 2016; Supplementary data S1). Trace element-to-calcium ratios represent the sample points, which were filtered for each specimen by setting a threshold at two-thirds of the highest sample density in Principal Component Analysis (PCA), following the method outlined by Coimbra et al. (2020). This method was implemented using a Python script (Supplementary data S2 following Miloikovitch, 2024) where missing and below-detection-limit values in the dataset were replaced by zeros, and the data standardized using the StandardScaler class from the Scikit-learn library. Each of the element-to-calcium ratios were plotted along the growth direction of the specimens resilifer with LOWESS smoothening with an interval of 0.05 (Supplementary data S3).

The element-to-calcium ratio sample points, obtained through LA-ICP-MS were analyzed using Principal Component Analysis, with sample points from each specimen (K/Pk/01-03 and K/Fl/15,38,57) enclosed within a 95% confidence ellipse (Supplementary data S4).

3.8.2 Comparison with CESM simulation and modern climate

Bartonian atmospheric pCO_2 is estimated to have ranged between ~550 and ~1200 ppm (Foster et al., 2017; CenCO$_2$PIP Consortium, 2023). Accordingly, the proxy-derived values are compared with two to four times the pre-industrial CO_2 concentration (2-4xPIC; 560-1120 ppm). We compared our reconstructions with outcomes from the CESM run at ~2° × 1° atmospheric and ~1° × 0.5° oceanic resolution under 2x and 4x pre-industrial CO_2 forcing. The simulations were spun up for 3500 years (2xPIC) and 4500 years (4xPIC), with additional sensitivity runs exploring modified orbital forcing relative to the baseline eccentricity-minimum case for 2xPIC scenario. Results were extracted from the CESM run for the area of interest, defined between 7-17° N and 65-75° E, corresponding to the paleogeographic position of the Kutch Basin during the late

Bartonian (van Hinsbergen et al., 2015; Montheil et al., 2026). Modern sea surface temperature (SST) and surface air temperature (SAT) data were obtained from the high-resolution NOAA OISST v2 (0.25° global grids) and CHIRTS (0.05° global grids) datasets at weekly resolution for 2010-2016 (Verdin et al., 2020). Precipitation data were acquired from CHIRPS (0.05° global grids) at weekly resolution for 2010-2024 (Funk et al., 2015). These datasets were used to generate weekly SST, SAT, and precipitation time series for Kutch (68-71.5° E, 22-24.5° N), Kerala (75-78° E, 6-10° N), and southern Bengal (86-90° E, 20-24° N), after which smoothed average curves were fitted to highlight temporal trends. Modern $\delta^{18}O_w$ values for rivers in these three regions at elevations below 80 m and near their mouths, together with marine surface water $\delta^{18}O_w$ data from the near-shore Arabian Sea, Indian Ocean, and Bay of Bengal, were compiled from Kirkels (2020) and the Global Seawater Oxygen-18 Database (LeGrande and Schmidt, 2006).

4 Results

4.1 Carbon isotope stratigraphy

The early Bartonian Harudi and late Bartonian Fulra Limestone record $\delta^{13}C_{org}$ in the range of -21.71 ‰ to -26.51 ‰, respectively (Table 1). The units overlying the Coquina Limestone of the Harudi Formation (~5 m) exhibit an increasing trend in $\delta^{13}C_{org}$ values, which becomes more pronounced in the Fulra Limestone (Table 1). The stratigraphic layer containing *P. kachchhensis* and *T. bulbiformis* (18-22 m from base) has $\delta^{13}C_{org}$ values around -23 to -24 ‰ (Table 1).

Height (m)	$\delta^{13}C_{org}$ VPDB (‰)	Height (m)	$\delta^{13}C_{org}$ VPDB (‰)
Harudi Formation		Harudi Formation	
0	-25.79	10.6	-24.90
0.3	-25.58	11.3	-24.27
0.6	-25.48	12	-24.62
0.9	-25.49	12.7	-24.63
1.2	-24.44	13.4	-24.73
1.5	-23.94	Fulra Limestone	
2.1	-24.45	14.1	-23.42
2.3	-24.63	14.8	-23.40
3.4	-24.34	15.5	-23.18
3.6	-23.25	16.2	-22.98
3.8	-24.10	17.6*	-23.33
4.0	-23.91	18.3*	-23.27
4.2	-24.71	19*	-23.74
4.8	-26.51	19.7*	-23.53
5.6	-26.20	20.4*	-23.86
6.0	-25.09	21.1	-24.80
6.8	-22.90	21.8	-23.85
7.2	-25.32	22.5	-24.51
8.0	-26.13	23.2	-23.72
8.4	-22.02	28.8	-23.39
8.6	-21.87	29.5	-22.68
8.8	-21.71	31.6	-23.19
9.2	-21.74	34.4	-22.53
9.9	-25.14		

Table 1. $\delta^{13}C_{org}$ values from bulk sediment samples from the basal Harudi Formation (early Bartonian) to Fulra Limestone (late Bartonian). *P. kachchhensis* horizon is marked by *.

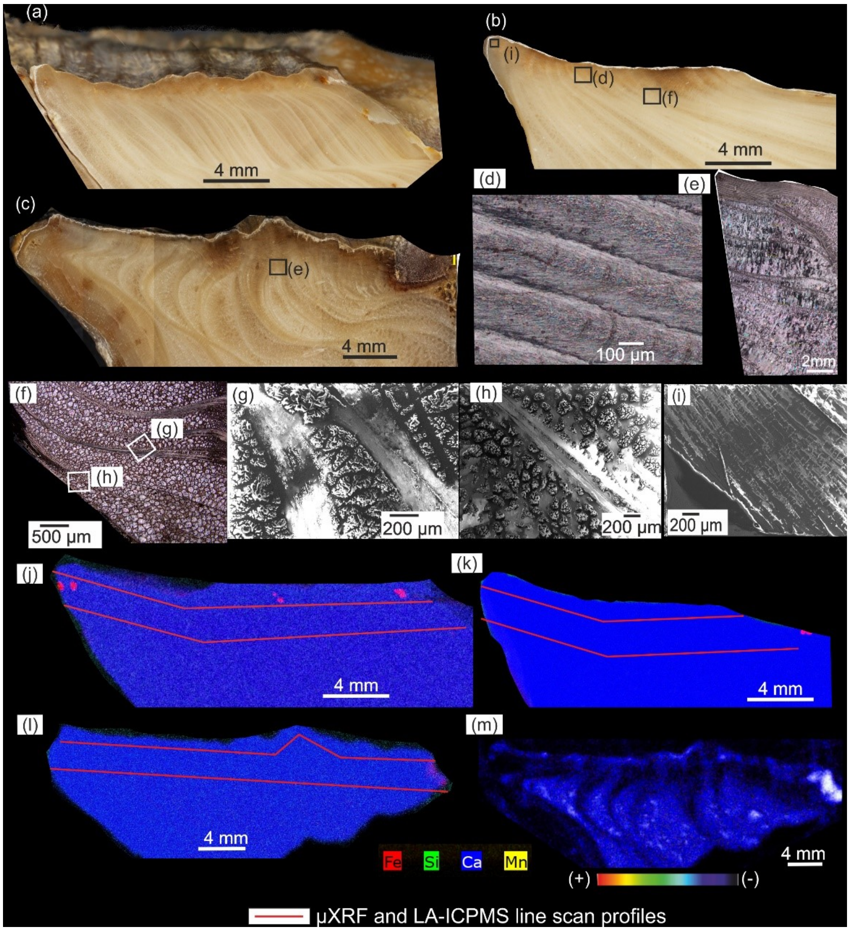

Figure 2. (a-c) Cross-sectional photograph of *Pycnodonte kachchhensis* shells: (a) K/Pk/01 (b) K/Pk/02 and (c) K/Pk/03; (d-f) Thin section microscopic images: (d) Foliated calcite from the resilifer zone of K/Pk/02; (e-f) Foliated and vesicular calcite in (e) K/Pk/03 and (f) K/Pk/02; (g-i) SEM images of foliated and vesicular calcite zones from K/Pk/02; (j-l) µXRF scanning map of Ca, Si, Mn and Fe (colour coded, red lines indicate the µXRF line scanning profile) of (j) K/Pk/01, (k) K/Pk/02 and (l) K/Pk/03; (m) Elemental heatmap of Fe in K/Pk/03.

4.2 Microscopy and µXRF elemental mapping of oyster shells

Two distinct colour zones are visible in the polished *Pycnodonte* thick-sections under normal light (Fig. 2a-c). Thin, light brown layers extend from the edge of the resilifer, while thicker bands of light yellowish to white layer are nearly absent at the resilifer's edge but become progressively more prominent further to the interior of the shell (Fig. 2a-c). In thin-sections, the thin dark layers near the resilifer edge exhibit a tightly bundled, foliated calcite structure (Fig. 2d-f). In contrast, the pale layers display a vesicular, honeycomb-like calcite texture with noticeable voids (Fig. 2e-f). Scanning electron microscopy (SEM) reveals a shallow relief with earthy texture within the honeycomb like structures, giving them a spongy and porous appearance (Fig. 2g-h; de Winter et al., 2018). Very thin regions with relatively lower relief mark boundaries between the honeycombs.

https://doi.org/10.5194/egusphere-2026-1393
Preprint. Discussion started: 14 April 2026

The foliated layers lack internal features, exhibiting a bladed, elongated, and fibrous morphology, clustered together in a subparallel arrangement (Fig. 2i).

Two shells of *P. kachchhensis* (K/Pk/01,02) are uniform in terms of relative abundance of Ca in the resilifer regions (Fig. 2j-k). The µ-XRF elemental map reveals a narrow zone (2 mm) along the edge of the K/Pk/03 resilifer with relatively higher Ca concentration, while rest of the shell has higher Fe and Mn concentrations (Fig. 2l-m). Those thin bands of high Ca content consist of foliated calcite as revealed by normal and scanning electron microscopy, while the rest of the shell, characterized by higher Fe concentration, consist of vesicular calcite (Fig. 2e).

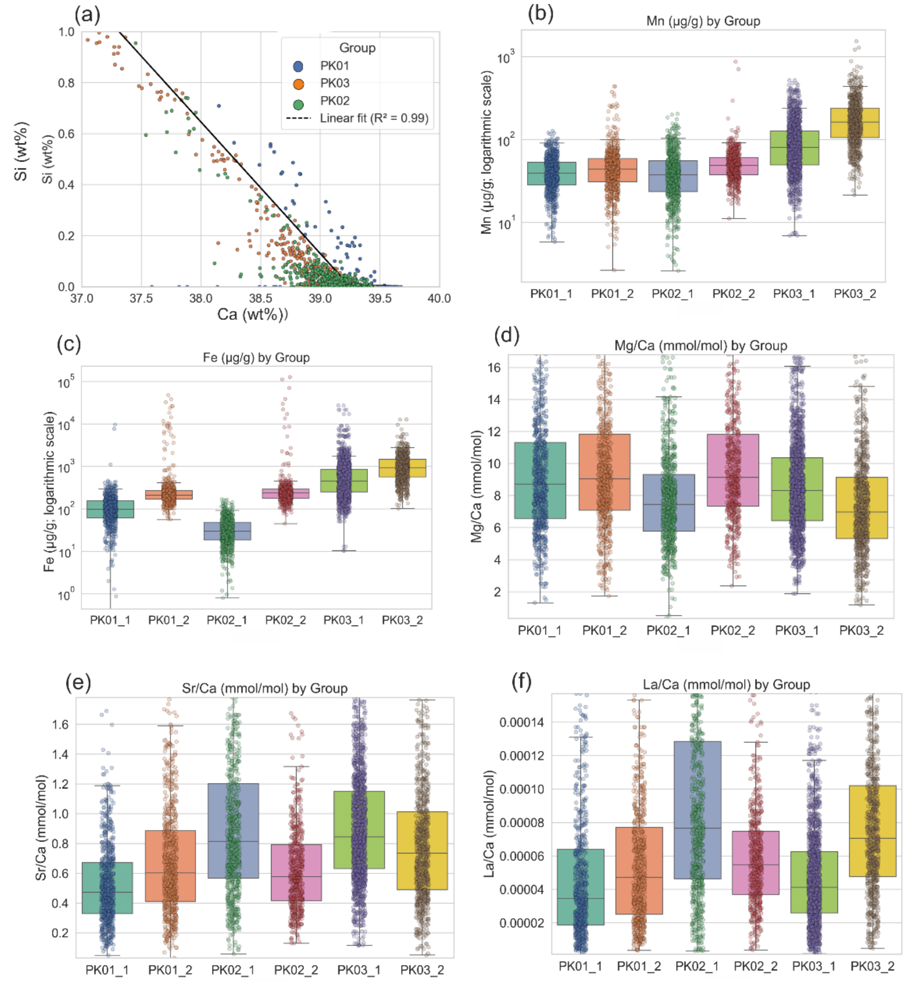

Figure 3. (a) Cross-plot between Ca (wt%) and Si (wt%) of all the sample points from the µ-XRF line scans of the pycnodont specimens (K/Pk/01-03). (b-f) Box and whisker plots of elements (Mn and Fe) and elements/Ca ratios (Mg/Ca, Sr/Ca and La/Ca) constituting the sample points from LA-ICP-MS line scans of all the analyzed pycnodont transects; PK01_1, PK02_1, PK03_1 indicate the resilifer-edge transects, PK01_2, PK02_2, PK03_2 indicate the transects away from the resilifer edges. Box and whisker plots of all the elements are shown in supplementary file Fig. S2.

4.3 Major, Trace and Rare Earth Element concentrations in oyster shells

Calcium exhibits an inverse relationship with silicon (Fig. 3a); thus, intervals characterized by lower Ca and elevated Si concentrations likely indicate structural defects and represent potential zones of diagenetic alteration (R^2=0.99, Fig. 3a). Mn and Fe concentrations in K/Pk/03 are much higher than in the other two shells (K/Pk/01,02), though other elements to Ca ratios remain almost within the same range (Figs. 3, S2). In the resilifer edge, transects of specimens K/Pk/01 and K/Pk/02, Mn and Fe rarely exceed 150 µg/g, with mean concentrations of 113-115 µg/g for Mn and 41-58 µg/g for Fe, (Figs. 3b-c, 4a-b). In contrast, K/Pk/03 shows consistently higher Mn and Fe concentrations, averaging 192 µg/g and 725 µg/g, respectively, particularly near the ventral end of the resilifer where Ca falls below 38.0 wt% and Si exceeds 0.3 wt% (Figs. 3a-b, 4c). Elevated concentrations of Mn and Fe are observed in areas with high Si and low Ca levels (Fig. 4). These datasets are included in Supplementary Table S2.

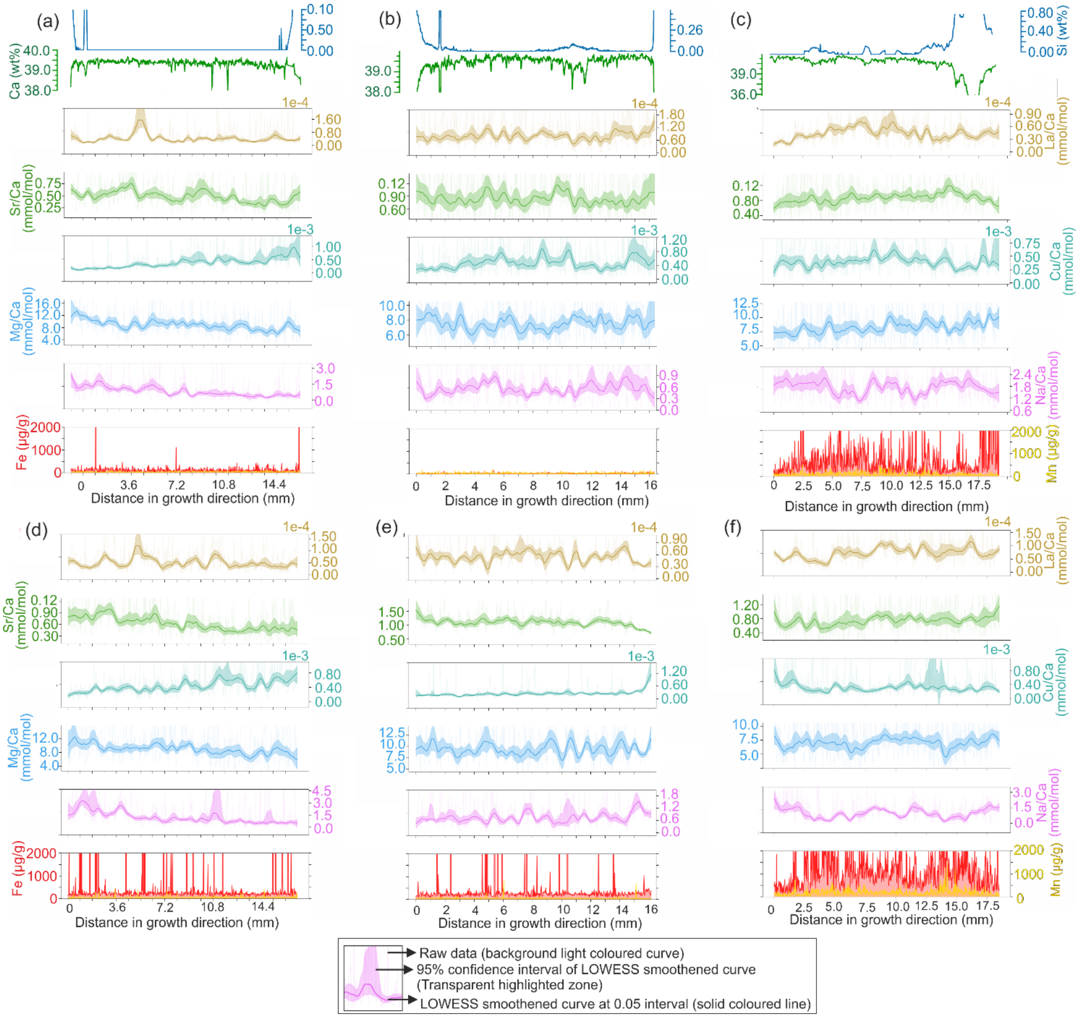

Figure 4. Plots of Ca and Si wt%, manganese (Mn) and iron (Fe) concentrations along with trace element-to-calcium ratios, measured along the growth axes of the resilifers in *P. kachchhensis* shells: (a-c) resilifer edge transects of (a)

K/Pk/01 (b) K/Pk/02 and (c) K/Pk/03; (d-f) transects 2mm away from the resilifer edges of (d) K/Pk/01, (e) K/Pk/02 and (f) K/Pk/03. Only one representative trace element-to-calcium ratio profiles from each element category (light metal, large ion lithophile elements, transition metals and rare earth elements) are shown. All trace element-to-calcium profiles is shown in supplementary file Fig. S4.

Periodic variations in trace element-to-calcium ratios are evident along the growth axes of the oyster specimens (Fig. 4; Table S2). In K/Pk/01, ratio profiles along both transects display either overall increasing or decreasing trends (Figs. 4a,d; S3-4). The trace element-to-calcium ratios can be grouped into three categories. Light elements (Na/Ca, Mg/Ca: LTE/Ca) show strong covariation in K/Pk/01 but weak correlations in K/Pk/02 (Figs. 4; S3). Transition metals (Ti/Ca, Ni/Ca, Cu/Ca, Zn/Ca: TMTE/Ca) constitute a second group characterized by strong internal covariation. A third group comprises large-ion lithophile elements (LILE: Sr, Ba) and REEs (La, Ce, Pr, Nd, Sm), clustered here as LRTE/Ca ratios, which shows the strongest correlations amongst them (Figs. 4; S3). Concentrations of Th, and U are too low to be considered for seasonal variability.

4.4 Carbon, oxygen and clumped isotope analysis

Stable isotope analyses of two *P. kachchhensis* specimens (K/Pk/01, K/Pk/02) yielded $\delta^{13}C_{cc}$ values ranging from 0.79 to 1.60 ‰ and $\delta^{18}O_{cc}$ values from -2.82 to -4.21 ‰ (Table 2). The shell of K/Pk/03 is excluded for stable isotope analysis because of high Mn and Fe concentration which points on potential diagenetic overprinting (Sect. 5.1; Figs. 3b-c, 4c-f; Mitra et al., 2025).

Specimen: K/Pk/01			Specimen: K/Pk/02		
Distance (mm)	$\delta^{13}C_{cc}$ VPDB (‰)	$\delta^{18}O_{cc}$ VPDB (‰)	Distance (mm)	$\delta^{13}C_{cc}$ VPDB (‰)	$\delta^{18}O_{cc}$ VPDB (‰)
0	1.6	-3.01	0	1.22	-3.01
1	1.15	-4.21	1	1.3	-3.01
2	1.32	-3.76	2	1.01	-3.33
3	1.39	-3.38	3	0.96	-3.5
4	1.28	-3.73	4	1.13	-3.32
5	1.33	-3.7	5	1.04	-3.22
6	1.57	-3.26	6	1.09	-3.04
7	1.52	-3.13	7	1.01	-3.41
8	1.33	-3.33	8	1.11	-3.28
9	1.35	-3.5	9	1	-3.36
10	1.38	-3.58	10	1.02	-3.24
11	1.4	-3.49	11	1.22	-2.95
12	1.49	-3.44	12	1.17	-2.82
13	1.55	-3.3	13	0.85	-3.18
14	1.42	-3.4	14	0.83	-3.12
15	1.47	-3.18	15	1.05	-3.15
16	1.44	-2.95	16	1.1	-3.33
17	1.23	-3.14			
18	1.23	-2.85			

Table 2. Isotope ($\delta^{13}C_{cc}$ and $\delta^{18}O_{cc}$) data from two specimens of *P. kachchhensis* (K/Pk/01 and K/Pk/02).

Clumped isotope analysis of independent check standards ETH-4, IAEA C1, and IAEA C2 measured alongside the samples yielded mean Δ_{47} values of 0.465±0.016 ‰, 0.296±0.012 ‰, and 0.627±0.016 ‰, respectively (Supplementary Table S4) that were within uncertainty of their accepted values (ETH-4: 0.4505±0.0035; IAEA C1: 0.3018±0.0025; IAEA C2: 0.6409±0.0030; see interlaboratory comparison study by Bernasconi et al., 2021). The Δ_{47} values of the unknown samples fall in an overall range of 0.562±0.008 ‰ to 0.574±0.008 ‰, corresponding to an estimated temperature range of $31^{+2.2}_{-2.1} - 36^{+2.8}_{-2.7}$ °C. Their calcuated $\delta^{18}O_w$ varies between $0.6^{+0.4}_{-0.4}$ and $1.6^{+0.6}_{-0.5}$ ‰ (Table 3).

Distance (mm)	$\delta^{13}C_{cc}$ VPDB (‰)	$\delta^{18}O_{cc}$ VPDB (‰)	$\delta^{18}O_{cc}$ VSMOW (‰)	$\Delta_{47\ \mathrm{I\text{-}DES90}}$	Δ_{47}-T (°C)	$\delta^{18}O_w$ VSMOW (‰)	No. of replicates
3	0.87±0.04	-3.26±0.1	27.56±0.11	0.562±0.007	$35.8^{+2.8}_{-2.7}$	$1.2^{+0.5}_{-0.5}$	11
6	0.81±0.03	-3.04±0.06	27.79±0.07	0.574±0.006	$31.3^{+2.2}_{-2.1}$	$0.6^{+0.4}_{-0.4}$	9
8	0.79±0.03	-3.24±0.06	27.58±0.06	0.568±0.010	$33.5^{+3.7}_{-3.6}$	$0.8^{+0.7}_{-0.7}$	9
12	0.89±0.02	-2.84±0.03	27.99±0.03	0.562±0.008	$35.6^{+3.0}_{-2.9}$	$1.6^{+0.6}_{-0.5}$	11

Table 3. Clumped isotope results with estimated temperature (Δ_{47}-T) and $\delta^{18}O_w$ from specimen K/Pk/02. Δ_{47}-T calculated with temperature relationship of Anderson et al., 2021; $\delta^{18}O_w$ with temperature relationship of Kim and O'Neil, 1997; displayed uncertainties are 95% CI.

5 Discussion

5.1 Preservation of the shells

Inferring seasonally resolved palaeoclimate and rapid environmental changes of Bartonian age, using fossil oysters requires verifying the preservation of the analyzed shells. The pycnodonts are composed of two types of calcite crystals: foliated calcite, which forms the inner surface (i.e cross-sectional edge) of the resilifer and extends inward as thin channels (Fig. 2d-f); and vesicular calcite, which occupies a larger portion of the shell interior as the oyster grows but is nearly absent near the resilifer edges (Fig. 2). The honeycomb-like vesicular calcite in pycnodonts is more prone to diagenetic alteration, as indicated by higher Fe incorporation, due to its porous structure compared to the more compact foliated calcite (Figs. 2-4; de Winter et al., 2018). The transect away from the resilifer edge contains higher concentration of Mn and Fe in a wider zone with respect to the edge, which is observed in all the specimens (Fig. 4d-f). The area closest to the resilifer margin in pycnodonts contains the most pristine calcite, making it ideal for sclerochronological analysis due to its dominance of well-preserved foliated calcite. Although Fe concentrations are higher in K/Pk/03 and in transects taken away from the resilifer edges in K/Pk/01-02, the overall elemental distributions particularly for Mg, LILE and REEs remain largely consistent across samples (Figs. 4, S4). Notable exceptions include trace elements such as Na, Ti, Ni and Zn, which show some degree of variability which can be an effect of dissolution and reprecipitation (Brand and Veizer, 1980; Casella, 2019). Stable isotope values remained almost the same for both the K/Pk/01 and 02 (Table 2) despite the first specimen having relatively higher Fe concentration in the second transect (Fig. 4). Thus, only the shell of K/Pk/02 was used for clumped isotope and trace element-to-calcium analysis to avoid any potential diagenetic effect, which might alter the temperature and seasonal signal in the two other shells.

5.2 Stratigraphic age correlation

The Fulra Limestone, which hosts *P. kachchhensis* lacks precise chronological constraints beyond biostratigraphy i.e. SBZ17 and E12 which broadly spans approximately four million years (41-37 Ma; Figs. 1, 5). In the underlying Harudi Formation, a sharp negative carbon isotope excursion (CIE: ~2 ‰) coinciding with the lowest taxon range zone of SBZ17 and E11 biostratigraphic interval has been interpreted to reflects the MECO event at ~41 Ma (Fig. 5). Although the MECO is not typically marked by a major CIE from oceanic foraminiferal chemostratigraphy, records from terrestrial to marginal marine settings including the Kutch Basin, document excursions of ~1-2 ‰ in $\delta^{13}C_{org}$ (Khanolkar et al., 2017; Ma et al., 2024). The Fulra Limestone, conformably lying over Harudi Formation not only lacks any carbon isotope excursions (CIE) but also has relatively higher $\delta^{13}C_{org}$ values comparative to early Bartonian units, consistent with the global trend of increasing $\delta^{13}C$ during the late Bartonian (Table 1; Fig. 5; Henehan et al., 2020; Ma et al., 2024). Consequently, the *Alveolina* wackestone interval, from where *P. kachchhensis* was collected, is interpreted to represents late Bartonian based on relative chemostratigraphic position and biostratigraphic correlation (Fig. 5).

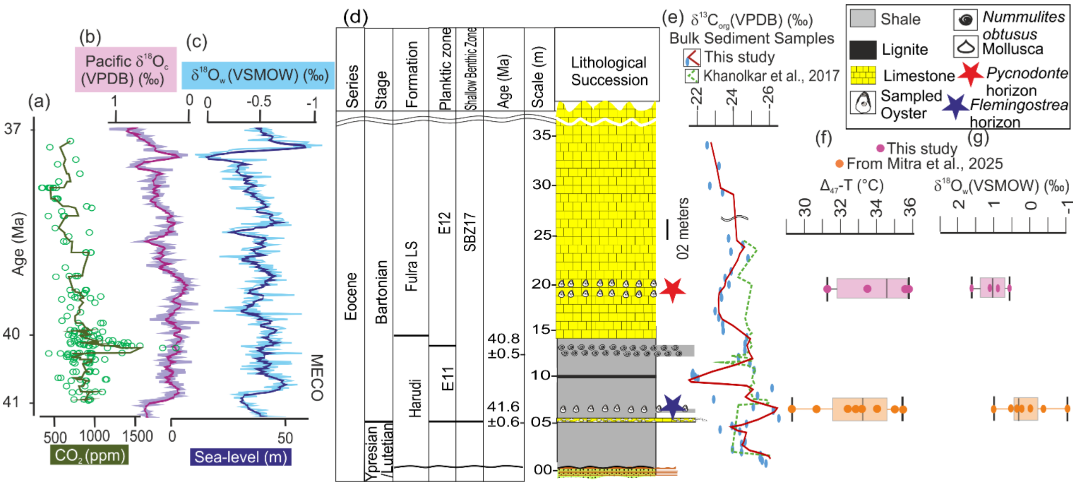

Figure 5. (a) Atmospheric pCO₂ estimates (symbols) with five-point moving average (after CenCO₂PIP Consortium, 2023) (b-c) Records from the Pacific Ocean cores with five-point moving average (after Miller et al., 2020): (b) Pacific $\delta^{18}O_{cc}$ stratigraphy of Eocene based on *Cibicidoides* spp., (c) Sea level and $\delta^{18}O_w$ values; (d) Lithostratigraphic section of the Bartonian sequence in the Kutch Basin, with (e) bulk sediment $\delta^{13}C_{org}$ stratigraphy with three point moving average from this study along with $\delta^{13}C_{org}$ stratigraphy from Khanolkar et al., 2017, (f) estimated temperatures and (g) $\delta^{18}O_w$ values from the respective stratigraphic horizons of early Bartonian *Flemingostrea* (Mitra et al., 2025) and late Bartonian and *Pycnodonte* (this study).

5.3 Palaeoenvironment

Sedimentological and paleoenvironmental analyses of the late Bartonian Fulra Limestone including facies, ichnology, foraminiferal assemblages, diagenetic features, and lithological associations indicate a lagoonal depositional setting at the stratigraphic level of *P. kachchhensis* (Srivastava and Singh, 2019; Banerjee et al., 2018; Das et al., 2024). Its occurrence within an *Alveolina* wackestone horizon further supports a low-energy inner-ramp habitats of alveolinids and pycnodonts (Ahmad et al., 2014; Kakemem et al., 2023; Moneer et al., 2024).

5.3.1. MECO to post-MECO environmental shift

Previous results from the MECO (Mitra et al., 2025) compared to the post-MECO data reported here sheds light on paleoenvironmental impact of this major climate event. The early Bartonian Harudi Formation of the Kutch Basin with shale-dominated lithology is followed by the abrupt transition to a thick carbonate platform deposition in the late Bartonian Fulra Limestone (Figs. 1d, 5d; Biswas, 1992; Das et al., 2024; personal field observations). This shift is associated with contrasting $\delta^{13}C_{org}$, $\delta^{18}O_w$ and $\delta^{18}O_{cc}$ signatures between the early and late Bartonian (Figs. 5, 6a; Mitra et al., 2025), the late Bartonian dataset reveals in average approximately 1 ‰ higher $\delta^{18}O_w$ (Fig. 5f-g). Based on benthic foraminifera *Cibicidoides* spp., which has a carbonate $\delta^{18}O_{cc}$ value of -0.5 to -1.5 ‰ (Fig. 5b, Lear et al., 2004; Cramer et al., 2011), the tropical seawater $\delta^{18}O_w$ value during the Bartonian (0 to -1 ‰) was lower than in modern times (0.2-0.5 ‰) in a relatively much higher pCO₂ condition (Fig. 5a-b; Schmidt et al., 1999; Tripati et al., 2014). The relatively high $\delta^{18}O_w$ values inferred from the *P. kachchhensis* shells (0.6-

1.6 ‰) likely reflect local high evaporation within a shallow, semi-restricted basin with limited exchange with the open ocean (Chamberlayne et al., 2021), similar to present day highly evaporative conditions of restricted tropical environments (McConnell et al., 2009: 2‰) where evaporative conditions enrich the restricted water mass with the heavy ^{18}O isotope (see Sect. 5.5.3). The relatively narrow $\delta^{18}O_{cc}$ range observed in our results (-2.82 to -3.5 ‰; Fig 6a) likely reflects the opposing effects of high temperatures (which lowers $\delta^{18}O_{cc}$) and elevated $\delta^{18}O_{w}$ (which increases $\delta^{18}O_{cc}$) since $\delta^{18}O_{cc}$ depends on both water $\delta^{18}O_{w}$ and temperature (Kim and O'Neil, 1997), resulting in dampened isotopic variability. However, before furthering these climate interpretations, other effects potentially affecting these isotopic values have to be considered, namely the depth of the preferred growth habitat and vital effects.

An alternative explanation for the isotope shift could be distinct preferred growth habitats between *Flemingostrea* and *Pycnodonte*, where the latter in this study preferred shallower lagoonal conditions that were influenced by annual to multiannual flooding events in generally dry atmospheric conditions. Seasonal variability, captured by changes in seasonal temperature and δ^{18}O values, decreases significantly with water depth; by approximately 2.9 °C per 1000 m in tropical regions (Xiao et al., 2023), and $\delta^{18}O_{w}$ values differing by 0.3-0.4 ‰ between depths of 150 and 500 m (Sengupta et al., 2013). However, we argue that the temperature of the *Pycnodonte* shells habitat in the shallow mixed-layer above the thermocline is typically less affected and yields robust relative SST estimates (Hayami and Kase, 1992; Diedrich, 2008; Prasad and Bahulayan, 1996; Moneer et al., 2024). Indeed, modern vertical temperature profiles from the surface to depth in analogous mixed layers of equatorial to temperate regions show limited gradients (John et al., 2013). This suggest that the records from the early Bartonian *Flemingostrea* that also likely inhabited shallow water depths (Mitra et al., 2025) may be compared to *Pycnodonte* shell records from the late Bartonian (Figs. 5-6).

Potential species-specific vital effects in element incorporation also have to be considered. Here, Principal Component Analysis (PCA) of trace element concentrations, including REE data further underscores the role of environmental factors (Fig. 6b). Three principal components (PC1, PC2 and PC3) explain 70.63% variance, of which the first component (PC1) solely explains 50.04% of the trace elements to calcium datapoints (Figs. 6b, S5). The plots exhibit distinct clustering, clearly differentiating pycnodonts (violet dots) from flemingostreas (red, blue and green dots) with PC1 in the x axis (Figs. 6b, S5; Mitra et al., 2025). Clustering of *F. pseudoflemingi* specimens by specific region (Mitra et al., 2025) points to environmental control of spatial variation, rather than vital effects (Piwoni-Piórewicz et al., 2017; Ricardo et al., 2017; Fig. 6b).

The PCA results can be further interpreted in terms of paleoenvironmental changes, in particular to distinguish open marine vs. riverine input. The strongest contributors to PC1 include La/Ca, Ce/Ca, Nd/Ca, Pr/Ca, and Sm/Ca, indicating the importance of light REEs signatures in differentiating these groups (Fig. S6). REEs in seawater primarily originate from atmospheric fallout, riverine input via continental weathering, and hydrothermal activity (Mouchi et al., 2020 and references therein), and thus marine water generally has low REE concentrations (Nothdurft et al., 2004). REE concentrations in the Fulra Limestone are relatively low and typical to marine settings (Srivastava and Singh, 2019; Chaudhuri et al., 2022). In oysters, REEs may derive from pore water or resuspended sediments as well (Haley et al., 2004; Crocket et al., 2018), leading to fluctuating relative abundances without clear temporal cyclicity (Mouchi et al., 2020). The low variability and very low concentrations of REEs in the *Pycnodonte* shells strongly indicate a marine environment with minimal freshwater influence. The distinct clustering of the late Bartonian *P. kachchhensis* suggests a geochemically more homogeneous environment compared to the early Bartonian *F. pseudoflemingi* specimens. We thus suggest the study site (23°30′23.56″N, 68°41′02.51″E) likely experienced minimal surface runoffs during the late Bartonian, leading to persistently elevated $\delta^{18}O_{w}$ values and limited seasonal hydrological variability in the restricted lagoon (Fig. 6c). These observations indicate a shift in Kutch from humid conditions (Saraswati et al., 2018) to increasingly evaporative environments from the early to late Bartonian, with both organisms recording isotopic signatures of the shallow mixed layer. Whether this transition reflects an overall climatic shift or a local environmental change is further discussed below (Sect. 5.5.2) in light of the comparison with climate simulations and seasonality interpretations.

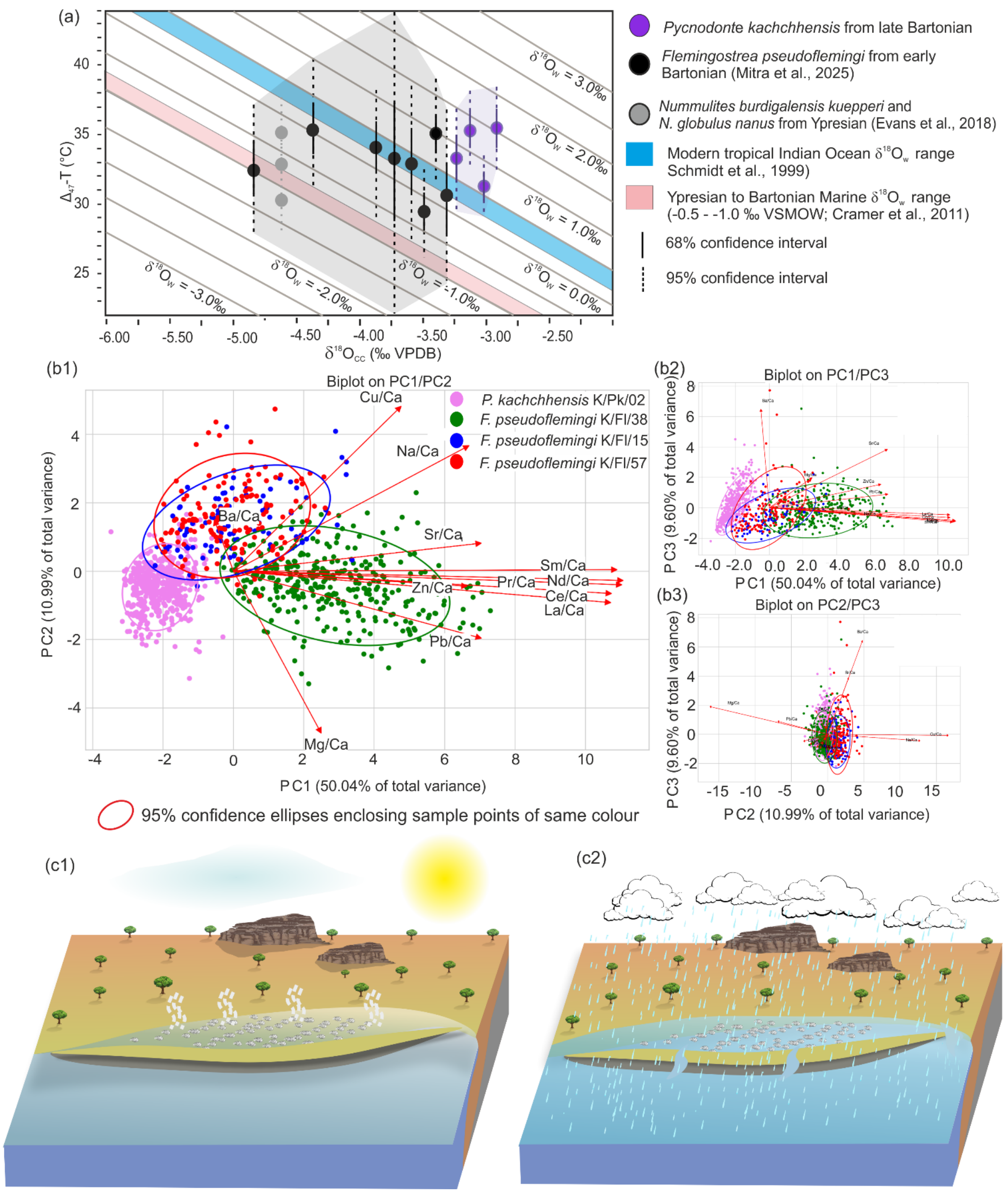

Figure 6. (a) Comparing Δ_{47}-T and $\delta^{18}O_w$ from the onset of MECO based on *Flemingostrea* shells (after Mitra et al., 2025) to post-MECO, based on *Pycnodonte kachchhensis* shells (37-41 Ma) of the Kutch Basin. Temperature (Δ_{47}-T) is plotted against $\delta^{18}O_{cc}$. (b) PCA plots based on trace element to Ca ratios from the analyzed specimens of *P. kachchhensis* (K/Pk/02) from lagoonal setting of Fulra Limestone and *F. pseudoflemingi* from shallow shelf setting of Harudi Formation. PCA plots with all the specimens are incorporated in the supplementary file. (c) Environmental model of the late Bartonian *P. kachchhensis* habitat in the lagoonal setting of the Fulra Limestone: (c1) evaporative conditions during the warmest months increased $\delta^{18}O_w$ values in a restricted lagoon; (c2) seasonal rainfall triggered seawater influx into the lagoon, leading to reduced temperature and evaporation and a consequent decrease in $\delta^{18}O_w$ values.

5.4 Seasonal effect on trace element incorporation

Clumped-isotope-derived SSTs can be compared to CESM simulated annual temperature variability to assign month-relative positions of the data points on the growth axis of K/Pk/02. This indicates that Δ_{47}-T values peak during April-May and attain their lowest levels in August-September and December-January, showing close consistency between the model results and the proxy based estimated values, and suggesting a minimum lifespan of ~2 years in the likely absence of growth cessations (Fig. 7). Accordingly, trace-element variability was evaluated along the growth axis using sub-annual climate model-based age estimates. Due to the small seasonal temperature variability in simulated Bartonian conditions for India, trace element variability in the shells may be interpreted as primarily influenced by the precipitation-evaporation cycle, which governed elemental concentrations in the water. The three elemental groups of light elements, transition metals, and large ion lithophiles and REE (LTE, TMTE and LRTE) exhibit consistent intra-group variability across all specimens transects, among which the LRTE/Ca pattern is consistent and the strongest (Fig. 7).

The Na/Ca ratio profile exhibits clear annual cyclicity, slowly increasing from March to August, the warmest months, then rapidly declining (Fig. 7). It indicates elevated evaporation, supported by higher $\delta^{18}O_w$ values in those months, raising Na^+ and salinity (Golan et al., 2016) during the warmest phase of a year. Modern oyster and planktonic foraminifera Na/Ca ratios correlate with salinity rather than temperature, supporting their use as paleo-salinity proxies. For example, seasonal *Crassostrea gigas* shells show elevated Mg/Ca, Na/Ca, and Sr/Ca during warm, high-salinity periods (Higuera-Ruiz and Elorza, 2009), corroborated by planktonic foraminifera and oysters (Mezger et al., 2016; Hauzer et al., 2018; Rucker and Valentine, 1961). Rapid declining trend of Na/Ca profile conforms with decreasing Na^+ concentration with freshwater influx by rainfall and decreasing salinity in parallel. Mg/Ca profiles, commonly interpreted as a paleotemperature proxy in oyster shells (Surge and Lohmann, 2008; Bougeois et al., 2014; Durham et al., 2017), does not covary in the pycnodonts with seasonal temperature and/or rainfall dynamics (Fig. 7). It is affected by salinity, water Mg/Ca ratio, growth, metabolism, and ontogeny (Putten et al., 2000; Schöne et al., 2010; Freitas et al., 2009; Mouchi et al., 2013). This highlights Mg/Ca profiles limitations in restricted, evaporative or freshwater-influenced environments (Tynan et al., 2017). Transition metals such as Cu are incorporated into shells from suspended and dissolved phases, modulated by physiology and environment (Huanxin et al., 2000). Because Cu uptake into oyster shells is generally favoured in lower salinity conditions (Huanxin et al., 2000), we interpret elevated Cu/Ca ratios during monsoon and post-monsoon months to indicate a strong salinity control on Cu incorporation. In contrast, enhanced summer evaporation increases salinity, resulting in the lowest Cu/Ca concentrations (Fig. 7). Increased Ba/Ca ratio is commonly associated with blooms of specific phytoplankton species, typically occurring in modern spring (Goodwin et al., 2013; Poitevin et al., 2020; Fröhlich et al., 2022). In this study, lower values of Ba/Ca are noticed during the warmest months and reach their highest values in the preceding periods, conforming to the modern observations (Fig. 7). Co-variation of Ba/Ca and Sr/Ca with REEs such as La, Ce, Pr, Nd, and Sm suggests that the REEs are also influenced

https://doi.org/10.5194/egusphere-2026-1393
Preprint. Discussion started: 14 April 2026

by phytoplankton dynamics. Seasonal influences are evident, with peak concentrations of a few trace elements typically observed during the spring to summer months in modern oysters as well, likely due to increased phytoplankton productivity and/or enhanced fluvial input enriched in trace metals (Liu et al., 2021). While REE incorporation is generally minimally affected by seasonality within a 5-20 °C range (Mouchi et al., 2020), the significantly higher temperatures (30-36 °C) during the late Bartonian India likely influenced REE uptake.

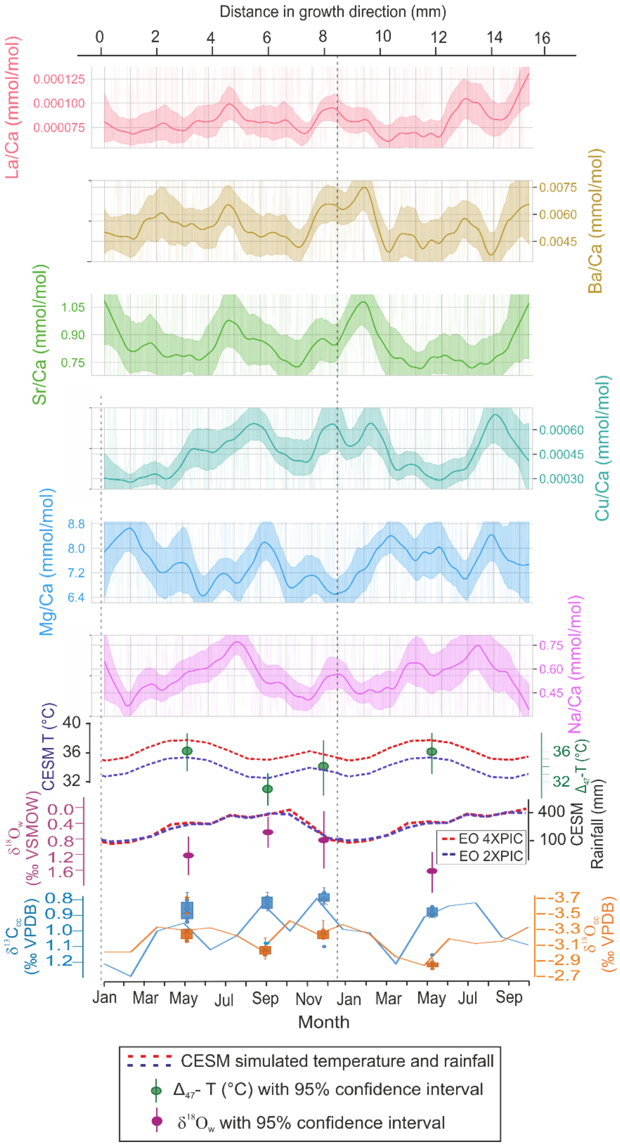

Figure 7. Trace element-to-Ca ratio profiles along the growth axis of K/Pk/02 are plotted together with stable isotope data, estimated Δ_{47}-T and $\delta^{18}O_w$ values, and CESM-simulated annual temperature and rainfall variations. The Δ_{47}-T temperatures along the growth axis are compared with the model-simulated temperature variability, and the trace-element profiles are subsequently evaluated to assess the presence of seasonal signals.

https://doi.org/10.5194/egusphere-2026-1393
Preprint. Discussion started: 14 April 2026

5.5 Palaeoseasonality

Clumped isotope thermometry reveals a relatively narrow temperature range of $31^{+2.2}_{-2.1} - 36^{+2.8}_{-2.7}$ °C (Figs. 6a, 7). By sampling aliquots from the higher and lower extreme points of $\delta^{18}O_{cc}$ curve, we interpret the estimated palaeotemperatures to capture both the warm and cool seasonal extremes as recorded in the shell.

The limited seasonal temperature variability and the estimated $\delta^{18}O_{w}$ (range of ~1‰: $0.6^{+0.4}_{-0.4} - 1.6^{+0.6}_{-0.5}$ ‰) explain the minimal seasonal fluctuations observed in $\delta^{18}O_{cc}$ (range of 0.5‰: 0.79 - 1.3‰), suggesting suppressed seasonality during shell growth (Fig. 7). The colder temperatures coincide with depleted $\delta^{18}O_{w}$, which we interpret as a result of increased freshwater input or sea-water influx with relatively lower $\delta^{18}O_{w}$ (-0.5 to -1 ‰; Cramer et al., 2011), and/or decreased evaporation. However, palaeoenvironmental reconstructions (Sect. 5.3) showing very low concentrations of trace elements and REEs (Fig. 6b) suggest limited terrestrial freshwater input, thereby pointing to a dominant influence of direct rainfall in the region and marine water exchange during periods of precipitation exceeding evaporation (Fig. 6c). The warmer season recorded in the oyster shell shows enrichment in $\delta^{18}O_{w}$, probably due to a higher rate of evaporation than precipitation (Fig. 7).

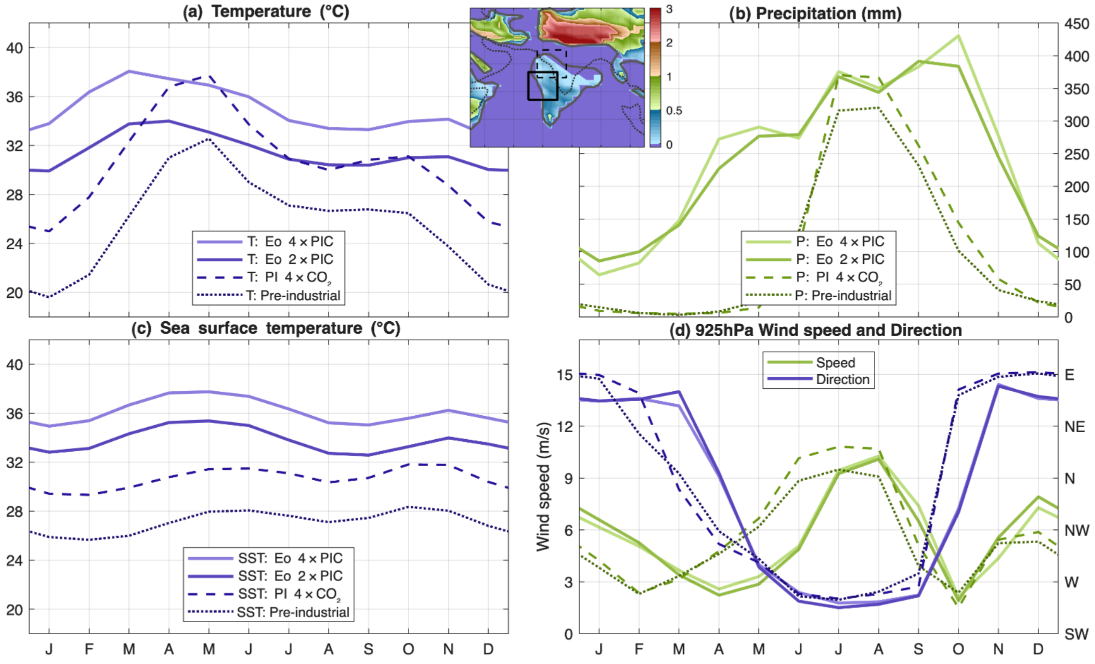

Figure 8. CESM monthly outputs. The inset shows model topography (km) and coastlines defined by the 0.5 land-fraction contour; the pre-industrial (PI) coastline is indicated by the dotted line. The solid box denotes Bartonian Kutch (7-17° N, 65-75° E) simulated under 2x (late Bartonian) and 4x (MECO, early Bartonian) pre-industrial pCO₂ (PIC) and CH₄, while the dotted box denotes modern Kutch (15-25° N, 68-78° E) under pre-industrial and simulated 2,4×PIC conditions (following Baatsen et al., 2020). Panels show (a) 2 m surface air temperature, (b) precipitation, (c) sea-surface temperature, and (d) wind speed and direction at 925 hPa.

5.5.1 Comparison with CESM simulations

We interpret the seasonal patterns in our records compared to the climate simulations. Our reconstructed late Bartonian palaeoequatorial SSTs of ~31-36 °C were consistently 2-3 °C lower than those simulated in 4xPIC CESM simulations (~35-38 °C) and falls in the range of 2xPIC simulations (32-35.5 °C; Figs. 8-9, S7; Baatsen et al., 2020). Both the model and proxy records indicate similarly low seasonal temperature variability (Figs. 7, 8a,c). Proxy-based reconstructions show higher $\delta^{18}O_w$ values during the warmest months (i.e ~ May), suggesting enhanced evaporation relative to precipitation (Fig. 8a-c). Although evaporation is influenced by multiple factors such as temperature, wind speed, specific humidity, dew point, and cloud cover (Su et al., 2015; Zhang and Emanuel; 2016), the combination of high atmospheric temperature and decreasing sea-level pressure during March-May months (Figs. 9; S7) implies elevated latent heat flux and, therefore, maximum evaporation (Fig. 8). Moist winds from the western coast reached central India, resulting in relatively higher summer precipitation there compared to the west coast (Figs. 9c-d; S7). According to the model, precipitation peaks in the modern monsoon to post-monsoon months (July-October), coinciding with the influx of strong moisture-rich south-westerly winds over the Kutch region, very similar to modern monsoon (Figs. 8b,d, 9f). Outside the summer and monsoon interval, CESM simulations indicate moderate precipitation even in modern winter months (November-February) in Bartonian Kutch (Figs. 8b, 9). The northern seaway between India and Eurasia, which have served as a probable source of moisture contributing to precipitation till early Eocene (Tardif et al., 2023; Meijer et al., 2024), remained open till the middle Eocene and was likely closed by the late Eocene (Akhmetiev et al., 2012; Wadood et al., 2021; Montheil et al., 2026). CESM simulations indicate moisture transport from the northern relic-Tethys seaway and promoted rainfall in the Kutch region during post-monsoon to modern winter months of Eocene by northeasterly flowing wind (Figs. 9a-b, S7). Despite the absence of a pronounced low-pressure system in late Bartonian western India, rainfall persists during post-monsoon (Figs. 8, 9a-b), indicating that precipitation was not solely controlled by ITCZ dynamics. Proxy-derived lower $\delta^{18}O_w$ values (0.6-0.8‰) during September-December (Fig. 7) indicates sustained precipitation during monsoon and post-monsoon periods, consistent with model results. Rainfall was thus likely influenced by palaeogeographic factors, including Tibetan Plateau uplift (Farnsworth et al., 2019; Abhik et al., 2026) and open seaways in northern India (Figs. 1a, 9; Montheil et al., 2026) that enabled sustained moisture supply independent of classic monsoonal forcing (Figs. 9, S7), consistent with a nascent monsoonal regime with low temperature variability. Later tectonic events like the Paratethys Sea retreat, along with the Arabian platform emergence, East African and Anatolian-Iranian landforms strongly contributed to the intensification of the South Asian Monsoon evident today (Tardif et al., 2023; Sarr et al., 2022).

5.5.2 Comparison with early Bartonian

Our proxy records indicate limited change in seasonal temperature variability that remain weak from the early to late Bartonian, with comparable temperature ranges (29-36 °C and 31-36 °C, respectively; Fig. 5f) and minor cooling during peak rainfall months (Figs. 7, 8a-b; Mitra et al., 2025). While post-monsoon rainfall signals are not prominent in the early Bartonian, they become more evident in the late Bartonian (Figs. 7, 8). This is consistent with CESM simulations indicating little difference in annual climate variability, aside from a modest (~2 °C) warming during the MECO (Fig. 8). Despite atmospheric pCO_2 being substantially higher during the MECO (~4xPIC) compared to post-MECO (~2-3xPIC; Fig. 5a; Henehan et al., 2020; CenCO$_2$PIP Consortium, 2023), model simulations from earlier studies further show that a reduction in pCO_2 from 1120 to 560 ppm had minimal influence on northward summer ITCZ migration and monsoon-like seasonality during the Eocene (Tardif et al., 2023). This is consistent with proxy evidence indicating that pCO_2 primarily affects northern hemisphere mid to high latitude seasonality and monsoons but exerts little control in equatorial India (Toumoulin et al., 2022; Meijer et al., 2024). The limited changes in our proxy records also suggest that the paleogeographic configuration, another major driver of South Asian climate, has remained relatively stable despite the fast Indian plate motion and its ongoing collision with Asia (Westerweel et al., 2025). This is consistent with the paleogeographic reconstruction, in particular the persistence of an open Tethys to its north until the latest Eocene (Montheil et al., 2026; Fig. 8). Rather than global pCO$_2$ fluctuations or paleogeographic reorganisations, the observed increase in $\delta^{18}O_w$ values from the early to late Bartonian (Fig. 5g) more likely reflects a transition from shallow shelf to restricted lagoonal environments with enhanced evaporative influence (Sect. 5.3.1).

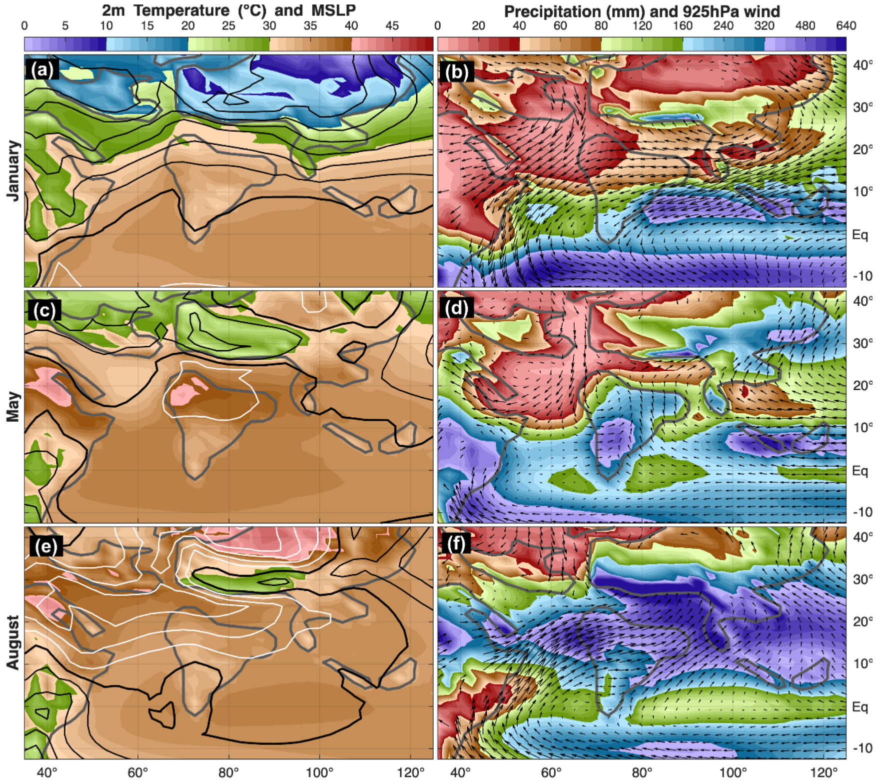

Figure 9. CESM outputs for the south Asian region at ~38 Ma under 2×PIC conditions in the months of January (post-monsoon rainfall month), May (peak summer) and August (monsoon): Left panels (a,c,e) show surface atmospheric air temperature at 2 m (shading) and mean sea level pressure (MSLP at 2.5 hPa intervals, white if <1000 hPa, thick black line at 1000 and 1020 hPa); Right panels (b,d,f) indicate precipitation (shading) and wind speed (length of arrows) and direction at 925 hPa.

5.5.3 Comparison with modern seasonality

We investigate how to explain the observed elevated $\delta^{18}O_w$ values relative to typically lower values in modern monsoons. While $\delta^{18}O_w$ of the Arabian Sea, Bay of Bengal and the Indian Ocean today remain higher than river water throughout the year, coastal and lagoonal systems on the eastern India show strong monsoonal $\delta^{18}O_w$ depletion linked to freshwater influx (Fig. 10; Singh et al., 2010; Colonese et al., 2017). The monsoonal rainfall in India exhibits significantly lower $\delta^{18}O_w$ (-6 to -10 ‰)

values compared to precipitation during other seasons, and distinctly lower than those of freshwater and marine sources (Rai et al., 2014; Jeelani et al., 2018). By analogy, the elevated $\delta^{18}O_w$ values observed in our study reflect climatic conditions comparable to the highly evaporative modern Gulf of Kutch with ~1 ‰ depletion during rainfall (Fig. 10). Moreover, the values suggest an even more restricted environment, as they exceed both present-day and contemporaneous marine $\delta^{18}O_w$ levels comparable to modern lagoons where $\delta^{18}O_w$ is higher than surrounding ocean water (Blamart et al., 2002). We explore why our records yield low $\delta^{18}O_w$ variability relative to expected modern monsoons. Comparison with modern temperatures from the arid Kutch Basin of western India (the study site) and the southern Bengal region of eastern India (at comparable latitudes) reveals that both regions exhibit stronger seasonal temperature contrasts (SAT: $\Delta T \approx 12$ °C; SST: $\Delta T \approx 5$-6 °C), with both summers and winters cooler than Eocene estimates, and modern winters showing a particularly pronounced cooling relative to the coolest Eocene months (Fig. 10). A pronounced SST-SAT gradient characterizes modern Kutch, particularly during summer (Fig. 10a), whereas Bartonian India exhibits a much weaker gradient (Fig. 8a,c), implying reduced land-sea thermal contrast, which limits the large-scale advection of the ITCZ in late spring and early summer (Tardif et al., 2023). In contrast, a modern latitudinal analogue for Eocene Kutch in Kerala, India (6-10° N), exhibit Eocene-like small seasonal temperature variation with smaller SST to SAT gradient (Fig. 10b,e). Modern Kutch, Kerala and southern Bengal exhibit ~2 °C SST declines during the monsoon, a pattern mirrored in our Eocene records where temperature drops coincide with lower $\delta^{18}O_w$ values (Fig. 10).

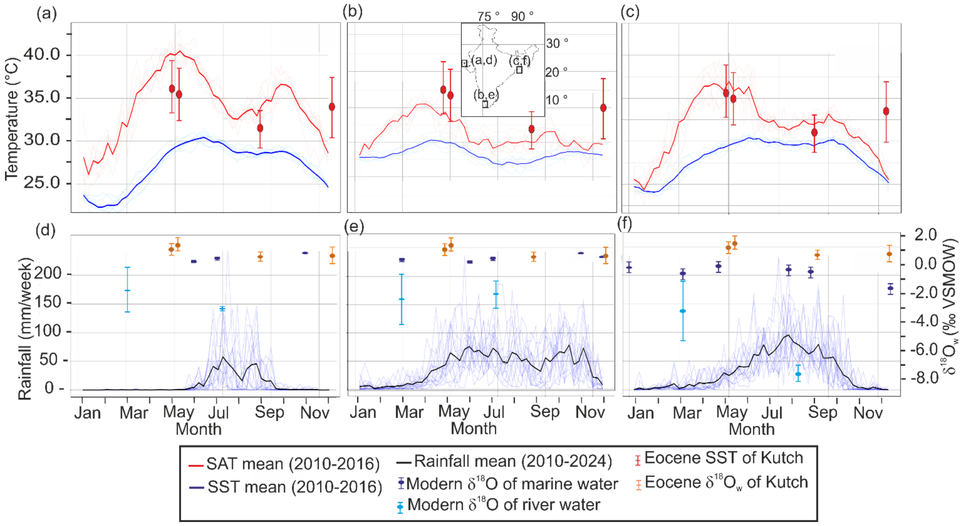

Figure 10. Late Bartonian sea-surface temperature (SST) and $\delta^{18}O_w$ are compared with modern SST, surface air temperature (SAT), and $\delta^{18}O_w$ of river water (below 80 m altitude) and marine water. Panels (a-c) show comparisons of Bartonian SST with modern SST and SAT from (a) Kutch, (b) Kerala, and (c) southern Bengal. Late Bartonian δ 18 O w values are compared with seasonal marine and river-water $\delta^{18}O_w$, from(d) Kutch, (e) Kerala, and (f) southern Bengal India: regions that experience the modern monsoon with differing intensity and timing. Source: Modern rivers-Kirkels, 2020; Modern Ocean: LeGrande and Schmidt, 2006.

We explore the significance of observed precipitations outside of typical monsoon season. In modern Kutch, as well as during the pre-industrial period, monsoon rainfall is largely confined to July-September and is substantially lower in magnitude compared to Eocene conditions (Figs. 8b, 10; Funk et al., 2015). A more open ocean configuration around the Indian subcontinent, combined with higher global temperatures and a lower latitudinal position relative to today, likely promoted enhanced and year-round rainfall during the Eocene. In contrast, southern Bengal receives precipitation during both the summer and the post-monsoon season in recent times. Bartonian Kutch, however, exhibits a rainfall regime comparable to that of modern Kerala, characterized by prolonged annual precipitation (Figs. 8b,9,10e). Thus, although a proto-monsoon was likely present in late Bartonian Kutch, it lacked the modern four-month confinement and had substantially weaker seasonal temperature differences than today as indicated by the reduced seasonal temperature variability record.

6 Conclusions

The Kutch Basin's palaeoequatorial climate during the late Bartonian is characterized by persistent warm temperature, with a shift towards evaporative conditions relative to early Bartonian, demonstrating remarkable temperature stability despite major Eocene climate events. This stable, warm climate, coupled with Tethyan Carbonate Ramp expansion, fostered formation of lagoon with the *Alveolina* wackestone at the basal Fulra Limestone. The basin's environmental evolution, from an early Bartonian shallow shelf with open marine and fluvial influence to a late Bartonian restricted lagoonal setting, is reflected in lower amount of trace element signatures of the oyster shells and exceptionally higher $\delta^{18}O_w$ with respect to Bartonian marine water.

Multi-year archives of the shells, supported by model simulations, reveal sustained year-round rainfall with peaks during summer monsoon months, without the pronounced seasonal temperature difference characterized by modern winter. Instead, the region likely maintained generally more extreme sea-surface temperatures than the present Gulf of Kutch, with rainfall-driven cooling events associated with typical reduced evaporation during monsoon and post-monsoon periods. Another difference with modern-like monsoonal patterns is rainfall during October-February outside the main monsoon season that may have been facilitated by the advection of moist air from the Tethys Seaway between India and Eurasia remaining open from the early to the late Bartonian. Overall, a nascent monsoon characterized by lower than modern persisted in equatorial India despite substantial CO_2 perturbations and the ongoing India-Asia collision during the late-middle Eocene.

Code and data availability

Bartonian atmospheric pCO_2 data were obtained from the CenCO$_2$PIP Consortium database (2023) available through the NOAA National Centers for Environmental Information at https://www.ncei.noaa.gov/pub/data/paleo/climate_forcing/trace_gases/Paleo-pCO2/product_files/. Modern daily sea surface temperature data were sourced from the NOAA Optimum Interpolation Sea Surface Temperature dataset (OISST v2) available at https://psl.noaa.gov/data/gridded/data.noaa.oisst.v2.highres.html. Daily atmospheric temperature data were obtained from the Climate Hazards Center InfraRed Temperature with Stations (CHIRTSdaily) dataset (https://data.chc.ucsb.edu/products/CHIRTSdaily/). Daily precipitation data were acquired from the Climate Hazards Group InfraRed Precipitation with Station data (CHIRPS v2.0) global daily dataset (https://data.chc.ucsb.edu/products/CHIRPS-2.0/global_daily/netcdf/p05/). Data for $\delta^{18}O_w$ of modern rivers were taken from Kirkels (2020), while modern ocean $\delta^{18}O_w$ values were obtained from LeGrande and Schmidt (2006). All the dataset generated in this study is included in the manuscript and the supplementary files, reposited at …………

CRediT authorship contribution statement

Aniket Mitra: Writing- original draft, Visualization, Formal analysis, Validation, Methodology, Investigation, Funding acquisition, Resources, Conceptualization, Data curation.

Steven Goderis: Writing- review and editing, Supervision, Methodology, Funding acquisition.

Niels J. de Winter: Writing- review and editing, Supervision, Methodology.

Michiel Baatsen: Writing- review and editing, Methodology, Software, Visualization, Data curation.

Béatrice A. Ledésert: Writing- review and editing, Validation, Funding acquisition.

Guillaume Dupont-Nivet: Writing- review and editing, Validation, Supervision.

Philippe Claeys: Writing- review and editing, Validation, Supervision, Resources, Funding acquisition, Conceptualization.

Inigo A. Müller: Writing- review and editing, Validation, Supervision, Formal analysis, Methodology, Project administration.

Declaration of competing interest

The authors declare they have no conflict of interest.

Funding Sources

Aniket Mitra acknowledges EUTOPIA Science and Innovation Fellowship of the European Union's Horizon 2020 programme under the Marie Skłodowska-Curie grant agreement No. 945380 for providing post-doctoral fellowship to A.M. and funding for the research work.

Acknowledgements

The authors acknowledge the laboratory facilities of ISTeP Laboratory, CY Cergy Paris University and AMGC Laboratory of the Vrije Universiteit Brussel. We thank Mr. David Verstraeten for the help and maintenance of the mass spectrometers, and Mr. Wim Borremans for aiding with the LA-ICP-MS analysis and processing of the data at VUB. Philippe Claeys acknowledges support from the Research Foundation Flanders (FWO) through grant no. G038022N. Philippe Claeys and Steven Goderis also acknowledge support from the VUB Strategic Research and the Research Foundation Flanders for the acquisition of the µ-XRF and LA-ICP-MS instruments (grant numbers I002122N). CESM simulations were performed at the SURFsara Dutch national computing facilities and were sponsored by NWO-EW (Netherlands Organisation for Scientific Research, Exact Sciences). These simulations were carried out within a programme of the Netherlands Earth System Science Centre (NESSC) and financially supported by the Ministry of Education, Culture and Science (OCW, grant no. 024.002.001). Guillaume Dupont-Nivet acknowledges support from ANR grant TIBETOP ANR-24-CE01-1073. Niels J. de Winter is supported through a VENI fellowship by the Netherlands Research Council (NWO) and funded by the "BETA Sectorplan" from the Dutch Ministry for Science and Education. Aniket Mitra and Béatrice A. Ledésert acknowledge funding support provided by the Chaire Éco-quartiers et Villes Durables through the CY Foundation.

Open Research

All data generated or analyzed during this study are included in the article and its Supplementary Material, available in the online repository of ....

References

Abhik, S., Capitanio, F. A., Goswami, B. N., Farnsworth, A., Clift, P. D., and Dommenget, D.: A brief history of Asian summer monsoon evolution in the Cenozoic era, npj Clim Atmos Sci, 9, 5, https://doi.org/10.1038/s41612-025-01259-7, 2026.

Ahmad, S., Kroon, D., Rigby, S., Hanif, M., Imraz, M., Ahmad, T., Jan, I. U., Ali, A., Zahid, M., and Ali, F.: Integrated paleoenvironmental, bio-and sequence-stratigraphic analysis of the late Thanetian Lockhart Limestone in the Nammal Gorge section, western Salt Range, Pakistan. Journal of Himalayan Earth Sciences, 47, 9-24, http://ojs.uop.edu.pk/jhes/article/view/1679, 2014.

Akagi, T. and Edanami, K.: Sources of rare earth elements in shells and soft-tissues of bivalves from Tokyo Bay, Marine Chemistry, 194, 55-62, https://doi.org/10.1016/j.marchem.2017.02.009, 2017.

Akhmetiev, M., Zaporozhets, N. I., Benyamovskiy, V. N., Aleksandrova, G., Iakovleva, A., and Oreshkina, T. V.: The Paleogene history of the Western Siberian seaway - a connection of the Peri-Tethys to the Arctic ocean, 2012.

Al-Aasm, I. S., and Veizer, J.: Diagenetic stabilization of aragonite and low-Mg calcite; I, Trace elements in rudists. Journal of Sedimentary Research 56, 138-152. https://doi.org/10.1306/212F88A5-2B24-11D7-8648000102C1865D, 1986.

Anderson, N. T., Kelson, J. R., Kele, S., Daëron, M., Bonifacie, M., Horita, J., Mackey, T. J., John, C. M., Kluge, T., Petschnig, P., Jost, A. B., Huntington, K. W., Bernasconi, S. M., and Bergmann, K. D.: A Unified Clumped Isotope Thermometer Calibration (0.5-1,100°C) Using Carbonate-Based Standardization, Geophysical Research Letters, 48, e2020GL092069, https://doi.org/10.1029/2020GL092069, 2021.

Anwar, D., Choudhary, A. K., Saraswati, P. K.: Strontium Isotope Stratigraphy of the Naredi Formation, Kutch Basin, India, in: Malarkodi, N., Keller, G., Reddy, A.N., Jaiprakash, B.C. (Eds.), Proceedings of XXIII Indian Colloquium on Micropaleontology and Stratigraphy and International Symposium on Global Bioevents in Earth's History. Geological Society of India, p. 0. https://doi.org/10.17491/cgsi/2013/63304, 2013.

Arndt, I., Bernecker, M., Erhardt, T., Evans, D., Fiebig, J., Fursman, M., Kniest, J., Renema, W., Schlidt, V., Staudigel, P., Voigt, S., and Müller, W.: 20,000 days in the life of a giant clam reveal late Miocene tropical climate variability, Palaeogeography, Palaeoclimatology, Palaeoecology, 661, 112711, https://doi.org/10.1016/j.palaeo.2024.112711, 2025.

Baatsen, M., von der Heydt, A. S., Huber, M., Kliphuis, M. A., Bijl, P. K., Sluijs, A., and Dijkstra, H. A.: The middle to late Eocene greenhouse climate modelled using the CESM 1.0.5, Climate of the Past, 16, 2573-2597, https://doi.org/10.5194/cp-16-2573-2020, 2020.

Banerjee, S., Khanolkar, S., and Saraswati, P. K.: Facies and depositional settings of the Middle Eocene-Oligocene carbonates in Kutch, Geodinamica Acta, 30, 119-136, https://doi.org/10.1080/09853111.2018.1442609, 2018.

Barrat, J.-A., Chauvaud, L., Olivier, F., Poitevin, P., and Rouget, M.-L.: Trace elements in bivalve shells: How "vital effects" can bias environmental studies, Chemical Geology, 638, 121695, https://doi.org/10.1016/j.chemgeo.2023.121695, 2023.

Bernasconi, S. M., Müller, I. A., Bergmann, K. D., Breitenbach, S. F. M., Fernandez, A., Hodell, D. A., Jaggi, M., Meckler, A. N., Millan, I., and Ziegler, M.: Reducing Uncertainties in Carbonate Clumped Isotope Analysis Through Consistent Carbonate-Based Standardization, Geochemistry, Geophysics, Geosystems, 19, 2895-2914, https://doi.org/10.1029/2017GC007385, 2018.

Bernasconi, S. M., Daëron, M., Bergmann, K. D., Bonifacie, M., Meckler, A. N., Affek, H. P., Anderson, N., Bajnai, D., Barkan, E., Beverly, E., Blamart, D., Burgener, L., Calmels, D., Chaduteau, C., Clog, M., Davidheiser-Kroll, B., Davies, A., Dux, F., Eiler, J., Elliott, B., Fetrow, A. C., Fiebig, J., Goldberg, S., Hermoso, M., Huntington, K. W., Hyland, E., Ingalls, M., Jaggi, M., John, C. M., Jost, A. B., Katz, S., Kelson, J., Kluge, T., Kocken, I. J., Laskar, A., Leutert, T. J., Liang, D., Lucarelli, J., Mackey, T. J., Mangenot, X., Meinicke, N., Modestou, S. E., Müller, I. A., Murray, S., Neary, A., Packard, N., Passey, B. H., Pelletier, E., Petersen, S., Piasecki, A., Schauer, A., Snell, K. E., Swart, P. K., Tripati, A., Upadhyay, D., Vennemann, T., Winkelstern, I., Yarian, D., Yoshida, N., Zhang, N., and Ziegler, M.: InterCarb: A Community Effort to Improve Interlaboratory Standardization of the Carbonate Clumped Isotope Thermometer Using Carbonate Standards, Geochem Geophys Geosyst, 22, https://doi.org/10.1029/2020gc009588, 2021.

Biswas, S.K.: Tertiary stratigraphy of Kutch. Journal of Paleontological Society of India, 37, 1-29, 1992.

Blamart, D., Escoubeyrou, K., Juillet-Leclerc, A., Ouahdi, R., and Lecomte-Finiger, R.: Composition isotopique d18O-d13C des otolithes des populations de poissons récifaux de Taiaro (Tuamotu, Polynésie française) : implications isotopiques et biologiques, Comptes Rendus. Biologies, 325, 99-106, https://doi.org/10.1016/S1631-0691(02)01419-1, 2002.

Bottjer, D. J., Roberts, C., and Hattin, D. E.: Stratigraphic and Ecologic Significance of Pycnodonte kansasense, a New Lower Turonian Oyster from the Greenhorn Limestone of Kansas, Journal of Paleontology, 52, 1208-1218, 1978.

Bougeois, L., de Rafélis, M., Reichart, G.-J., de Nooijer, L. J., Nicollin, F., and Dupont-Nivet, G.: A high resolution study of trace elements and stable isotopes in oyster shells to estimate Central Asian Middle Eocene seasonality, Chemical Geology, 363, 200-212, https://doi.org/10.1016/j.chemgeo.2013.10.037, 2014.

Bougeois, L., de Rafélis, M., Reichart, G.-J., de Nooijer, L. J., and Dupont-Nivet, G.: Mg/Ca in fossil oyster shells as palaeotemperature proxy, an example from the Palaeogene of Central Asia, Palaeogeography, Palaeoclimatology, Palaeoecology, 441, 611-626, https://doi.org/10.1016/j.palaeo.2015.09.052, 2016.

Brand, U., and Veizer, J.: Chemical diagenesis of a multicomponent carbonate system-1: Trace elements. J. Sediment. Res. 50, 1219-1236, 1980.

Briant, N., Le Monier, P., Bruzac, S., Sireau, T., Araújo, D. F., and Grouhel, A.: Rare Earth Element in Bivalves' Soft Tissues of French Metropolitan Coasts: Spatial and Temporal Distribution, Arch Environ Contam Toxicol, 81, 600-611, https://doi.org/10.1007/s00244-021-00821-7, 2021.

Budko, D. F., Lobus, N. V., and Vedenin, A. A.: Dataset on the content of major, trace, and rare-earth elements in the bottom sediments and bivalve mollusks of the Kara Sea (Arctic Ocean), Data in Brief, 36, 107087, https://doi.org/10.1016/j.dib.2021.107087, 2021.

Burioli, E. A. V., Squadrone, S., Stella, C., Foglini, C., Abete, M. C., and Prearo, M.: Trace element occurrence in the Pacific oyster *Crassostrea gigas* from coastal marine ecosystems in Italy, Chemosphere, 187, 248-260, https://doi.org/10.1016/j.chemosphere.2017.08.102, 2017.

Caldarescu, D. E., Sadatzki, H., Andersson, C., Schäfer, P., Fortunato, H., and Meckler, A. N.: Clumped isotope thermometry in bivalve shells: A tool for reconstructing seasonal upwelling, Geochimica et Cosmochimica Acta, 294, 174-191, https://doi.org/10.1016/j.gca.2020.11.019, 2021

Cardoso da Silva, P. S., Farias, W. de M., Gomez, M. R. B. P., Torrecilha, J. K., Rocha, F. R., Scapin, M. A., Garcia, R. H. L., Simone, L. R. L. de, Amaral, V. S. de, Vincent, M., Laurent, E., and Rudnicki-Velasquez, P.: Oyster shell element composition as a proxy for environmental studies, Journal of South American Earth Sciences, 134, 104749, https://doi.org/10.1016/j.jsames.2023.104749, 2024.

Casella, L. A.: Nano- and microstructural transformation processes during diagenesis of biogenic carbonates, PhD Thesis, Ludwig-Maximilians-Universität München, 2019.

Chamberlayne, B. K., Tyler, J. J., and Gillanders, B. M.: Controls Over Oxygen Isotope Fractionation in the Waters and Bivalves (Arthritica helmsi) of an Estuarine Lagoon System, Geochemistry, Geophysics, Geosystems, 22, e2021GC009769, https://doi.org/10.1029/2021GC009769, 2021.

Chaudhuri, S., De, S., Srivastava, H., Chattopadhyay, K., and Bhaumik, A. K.: Multiproxy analysis constraining climatic control over the Cenozoic depositional history of Kachchh, Western India, Geological Journal, 57, 3736–3768, https://doi.org/10.1002/gj.4511, 2022.

Coimbra, R., Huck, S., de Winter, N. J., Heimhofer, U., and Claeys, P.: Improving the detection of shell alteration: Implications for sclerochronology, Palaeogeography, Palaeoclimatology, Palaeoecology, 559, 109968, https://doi.org/10.1016/j.palaeo.2020.109968, 2020.

Colonese, A. C., Netto, S. A., Francisco, A. S., DeBlasis, P., Villagran, X. S., de Almeida Rocha Ponzoni, R., Hancock, Y., Hausmann, N., Eloy de Farias, D. S., Prendergast, A., Schöne, B. R., da Cruz, F. W., and Giannini, P. C. F.: Shell sclerochronology and stable isotopes of the bivalve *Anomalocardia flexuosa* (Linnaeus, 1767) from southern Brazil: Implications for environmental and archaeological studies, Palaeogeography, Palaeoclimatology, Palaeoecology, 484, 7-21, https://doi.org/10.1016/j.palaeo.2017.01.006, 2017.

Cramer, B. S., Miller, K. G., Barrett, P. J., and Wright, J. D.: Late Cretaceous-Neogene trends in deep ocean temperature and continental ice volume: Reconciling records of benthic foraminiferal geochemistry (δ^{18}O and Mg/Ca) with sea level history, Journal of Geophysical Research: Oceans, 116, https://doi.org/10.1029/2011JC007255, 2011.

Crocket, K. C., Hill, E., Abell, R. E., Johnson, C., Gary, S. F., Brand, T., and Hathorne, E. C.: Rare Earth Element Distribution in the NE Atlantic: Evidence for Benthic Sources, Longevity of the Seawater Signal, and Biogeochemical Cycling, Front. Mar. Sci., 5, https://doi.org/10.3389/fmars.2018.00147, 2018.

Das, M., Dasgupta, S., Srivastava, A., Rajkhowa, D., and Banerjee, S.: Ichnological response to the Middle Eocene Climatic Optimum (MECO) in the Bartonian deposits of Kutch Basin, India, Palaeogeography, Palaeoclimatology, Palaeoecology, 643, 112183, https://doi.org/10.1016/j.palaeo.2024.112183, 2024.

de Winter, N. J. and Claeys, P.: Micro X-ray fluorescence (μXRF) line scanning on Cretaceous rudist bivalves: A new method for reproducible trace element profiles in bivalve calcite, Sedimentology, 64, 231-251, https://doi.org/10.1111/sed.12299, 2017.

de Winter, N. J., Goderis, S., Dehairs, F., Jagt, J. W. M., Fraaije, R. H. B., Van Malderen, S. J. M., Vanhaecke, F., and Claeys, P.: Tropical seasonality in the late Campanian (late Cretaceous): Comparison between multiproxy records from three bivalve taxa from Oman, Palaeogeography, Palaeoclimatology, Palaeoecology, 485, 740-760, https://doi.org/10.1016/j.palaeo.2017.07.031, 2017a.

de Winter, N., Sinnesael, M., Makarona, C., Vansteenberge, S., and Claeys, P.: Trace element analyses of carbonates using portable and micro-X-ray fluorescence: Performance and optimization of measurement parameters and strategies., Journal of Analytical Atomic Spectrometry, https://doi.org/10.1039/c6ja00361c, 2017b.

de Winter, N. J., Vellekoop, J., Vorsselmans, R., Golreihan, A., Soete, J., Petersen, S. V., Meyer, K. W., Casadio, S., Speijer, R. P., and Claeys, P.: An assessment of latest Cretaceous *Pycnodonte vesicularis* (Lamarck, 1806) shells as records for palaeoseasonality: a multi-proxy investigation, Climate of the Past, 14, 725-749, https://doi.org/10.5194/cp-14-725-2018, 2018.

de Winter, N. J., Dämmer, L. K., Falkenroth, M., Reichart, G.-J., Moretti, S., Martínez-García, A., Höche, N., Schöne, B. R., Rodiouchkina, K., Goderis, S., Vanhaecke, F., van Leeuwen, S. M., and Ziegler, M.: Multi-isotopic and trace element evidence against different formation pathways for oyster microstructures, Geochimica et Cosmochimica Acta, 308, 326-352, https://doi.org/10.1016/j.gca.2021.06.012, 2021.

de Winter, N. J., Ullmann, C. V., Sørensen, A. M., Thibault, N., Goderis, S., Van Malderen, S. J. M., Snoeck, C., Goolaerts, S., Vanhaecke, F., and Claeys, P.: Shell chemistry of the boreal Campanian bivalve *Rastellum diluvianum* (Linnaeus, 1767) reveals temperature seasonality, growth rates and life cycle of an extinct Cretaceous oyster, Biogeosciences, 17, 2897-2922, https://doi.org/10.5194/bg-17-2897-2020, 2020.

Dhondt, A. V.: The unusual cenomanian oyster *Pycnodonte biauriculatum*, Geobios, 17, 53-61, https://doi.org/10.1016/S0016-6995(84)80156-4, 1984.

Diedrich, C. G.: The food of the miosirenAnomotherium langenwieschei (Siegfried) — indirect proof of seaweed or seagrass by xenomorphic oyster fixation structures in the Upper Oligocene (Neogene) of the Doberg, Bünde (NW Germany) and comparisons to modernDugong dugon (Müller) feeding strategies, Senckenbergiana maritima, 38, 59-73, https://doi.org/10.1007/BF03043869, 2008.

Dimri, A. P., Yasunari, T., Kotlia, B. S., Mohanty, U. C., and Sikka, D. R.: Indian winter monsoon: Present and past. Earth-science reviews, 163, 297-322, https://doi.org/10.1016/j.earscirev.2016.10.008, 2016.

Durham, S. R., Gillikin, D. P., Goodwin, D. H., and Dietl, G. P.: Rapid determination of oyster lifespans and growth rates using LA-ICP-MS line scans of shell Mg/Ca ratios, Palaeogeography, Palaeoclimatology, Palaeoecology, 485, 201-209, https://doi.org/10.1016/j.palaeo.2017.06.013, 2017.

Evans, D., Müller, W., Oron, S., and Renema, W.: Eocene seasonality and seawater alkaline earth reconstruction using shallow-dwelling large benthic foraminifera, Earth and Planetary Science Letters, 381, 104-115, https://doi.org/10.1016/j.epsl.2013.08.035, 2013.

Evans, D., Sagoo, N., Renema, W., Cotton, L. J., Müller, W., Todd, J. A., Saraswati, P. K., Stassen, P., Ziegler, M., Pearson, P. N., Valdes, P. J., and Affek, H. P.: Eocene greenhouse climate revealed by coupled clumped isotope-Mg/Ca thermometry, Proceedings of the National Academy of Sciences, 115, 1174-1179, https://doi.org/10.1073/pnas.1714744115, 2018.

Farnsworth, A., Lunt, D. J., Robinson, S. A., Valdes, P. J., Roberts, W. H. G., Clift, P. D., Markwick, P., Su, T., Wrobel, N., Bragg, F., Kelland, S.-J., and Pancost, R. D.: Past East Asian monsoon evolution controlled by paleogeography, not CO2, Science Advances, 5, eaax1697, https://doi.org/10.1126/sciadv.aax1697, 2019.

Fischer von Waldheim, G.: Lettre à M. le Baron de Férussac sur quelques genres de coquilles du Muséum Demidoff et en particulier sur quelques fossiles de la Crimée, *Bull. Soc. Imp. Nat. Moscou*, 8, 99-123, 1835.

Foster, G. L., Royer, D. L., and Lunt, D. J.: Future climate forcing potentially without precedent in the last 420 million years, Nat Commun, 8, 14845, https://doi.org/10.1038/ncomms14845, 2017.

Freitas, V., Cardoso, J. F. M. F., Santos, S., Campos, J., Drent, J., Saraiva, S., Witte, J. IJ., Kooijman, S. A. L. M., and Van der Veer, H. W.: Reconstruction of food conditions for Northeast Atlantic bivalve species based on Dynamic Energy Budgets, Journal of Sea Research, 62, 75-82, https://doi.org/10.1016/j.seares.2009.07.004, 2009.

Fröhlich, L., Siebert, V., Walliser, E. O., Thébault, J., Jochum, K. P., Chauvaud, L., and Schöne, B. R.: Ba/Ca profiles in shells of Pecten maximus - A proxy for specific primary producers rather than bulk phytoplankton, Chemical Geology, 593, 120743, https://doi.org/10.1016/j.chemgeo.2022.120743, 2022.

Funk, C., Peterson, P., Landsfeld, M., Pedreros, D., Verdin, J., Shukla, S., Husak, G., Rowland, J., Harrison, L., Hoell, A., and Michaelsen, J.: The climate hazards infrared precipitation with stations—a new environmental record for monitoring extremes, Sci Data, 2, 150066, https://doi.org/10.1038/sdata.2015.66, 2015.

Golan, R., Gavrieli, I., Ganor, J., and Lazar, B.: Controls on the pH of hyper-saline lakes - A lesson from the Dead Sea, Earth and Planetary Science Letters, 434, 289-297, https://doi.org/10.1016/j.epsl.2015.11.022, 2016.

Goodwin, D. H., Gillikin, D. P., and Roopnarine, P. D.: Preliminary evaluation of potential stable isotope and trace element productivity proxies in the oyster *Crassostrea gigas*, Palaeogeography, Palaeoclimatology, Palaeoecology, 373, 88-97, https://doi.org/10.1016/j.palaeo.2012.03.034, 2013.

Haley, B. A., Klinkhammer, G. P., and McManus, J.: Rare earth elements in pore waters of marine sediments, Geochimica et Cosmochimica Acta, 68, 1265-1279, https://doi.org/10.1016/j.gca.2003.09.012, 2004.

Hauzer, H., Evans, D., Müller, W., Rosenthal, Y., and Erez, J.: Calibration of Na partitioning in the calcitic foraminifer *Operculina ammonoides* under variable Ca concentration: Toward reconstructing past seawater composition, Earth and Planetary Science Letters, 497, 80-91, https://doi.org/10.1016/j.epsl.2018.06.004, 2018.

Hayami, I. and Kase, T.: 935. A new cryptic species of pycnodonte from Ryukyu islands : a living fossil oyster, TPPSJ, 1992, 1070-1089, https://doi.org/10.14825/prpsj1951.1992.165_1070, 1992.

Henehan, M. J., Edgar, K. M., Foster, G. L., Penman, D. E., Hull, P. M., Greenop, R., Anagnostou, E., and Pearson, P. N.: Revisiting the Middle Eocene Climatic Optimum "Carbon Cycle Conundrum" With New Estimates of Atmospheric pCO2 From Boron Isotopes, Paleoceanography and Paleoclimatology, 35, e2019PA003713, https://doi.org/10.1029/2019PA003713, 2020.

Higuera-Ruiz, R. and Elorza, J.: Biometric, microstructural, and high-resolution trace element studies in *Crassostrea gigas* of Cantabria (Bay of Biscay, Spain): Anthropogenic and seasonal influences, Estuarine, Coastal and Shelf Science, 82, 201-213, https://doi.org/10.1016/j.ecss.2009.01.001, 2009.

Höntzsch, S., Scheibner, C., Kuss, J., Marzouk, A. M., and Rasser, M. W.: Tectonically driven carbonate ramp evolution at the southern Tethyan shelf: the Lower Eocene succession of the Galala Mountains, Egypt, Facies, 57, 51-72, https://doi.org/10.1007/s10347-010-0229-x, 2011.

Huanxin, W., Lejun, Z., and Presley, B. J.: Bioaccumulation of heavy metals in oyster (Crassostrea virginica) tissue and shell, Environmental Geology, 39, 1216-1226, https://doi.org/10.1007/s002540000110, 2000.

Huber, M., and Goldner, A.: Eocene monsoons. Journal of Asian Earth Sciences, Asian Climate and Tectonics 44, 3-23, https://doi.org/10.1016/j.jseaes.2011.09.014, 2012.

Jeelani, G., Deshpande, R. D., Galkowski, M., and Rozanski, K.: Isotopic composition of daily precipitation along the southern foothills of the Himalayas: impact of marine and continental sources of atmospheric moisture, Atmospheric Chemistry and Physics, 18, 8789-8805, https://doi.org/10.5194/acp-18-8789-2018, 2018.

John, C. M. and Bowen, D.: Community software for challenging isotope analysis: First applications of 'Easotope' to clumped isotopes, Rapid Communications in Mass Spectrometry, 30, 2285-2300, https://doi.org/10.1002/rcm.7720, 2016.

Kachhara, R. P., Jodhawat, R. L., and Devi, K. B.: Molluscan biostratigraphy of the Palaeogene sediments around Lakhpat, Kachchh, Gujarat, India, J. Palaeontol. Soc. India, **56**, 17-28, 2011.

Kakemem, U., Cotton, L. J., Hadavand-Khani, N., Fallah-Bagtash, R., Thibault, N., and Anderskouv, K.: Litho- and biostratigraphy of the early Eocenelarger benthic foraminifera-dominated carbonates of the central Tethys domain, Zagros Foreland Basin, SW Iran, Sedimentary Geology, 455, 106477, https://doi.org/10.1016/j.sedgeo.2023.106477, 2023.

Kaskes, P., Déhais, T., de Graaff, S. J., Goderis, S., and Claeys, P.: Micro-X-ray fluorescence (µXRF) analysis of proximal impactites: High-resolution element mapping, digital image analysis, and quantifications, in: Large Meteorite Impacts and Planetary Evolution VI, vol. 550, edited by: Reimold, W. U. and Koeberl, C., Geological Society of America, 0, https://doi.org/10.1130/2021.2550(07), 2021.

Khanolkar, S. and Saraswati, P. K.: Ecological response of shallow-marine foraminifera to early Eocene warming in equatorial India, Journal of Foraminiferal Research, 45, 293-304, https://doi.org/10.2113/gsjfr.45.3.293, 2015.

Khanolkar, S. and Saraswati, P. K.: Eocene foraminiferal biofacies in Kutch Basin (India) in context of palaeoclimate and palaeoecology, J. Palaeogeogr., 8, 21, https://doi.org/10.1186/s42501-019-0038-2, 2019.

Khanolkar, S., Kumar Saraswati, P., and Rogers, K.: Ecology of foraminifera during the middle Eocene climatic optimum in Kutch, India, Geodinamica Acta, 29, 181-193, https://doi.org/10.1080/09853111.2017.1300846, 2017.

Kim, S.-T. and O'Neil, J. R.: Equilibrium and nonequilibrium oxygen isotope effects in synthetic carbonates, Geochimica et Cosmochimica Acta, 61, 3461-3475, https://doi.org/10.1016/S0016-7037(97)00169-5, 1997.

Kim, S.-T., O'Neil, J. R., Hillaire-Marcel, C., and Mucci, A.: Oxygen isotope fractionation between synthetic aragonite and water: Influence of temperature and Mg2+ concentration, Geochimica et Cosmochimica Acta, 71, 4704-4715, https://doi.org/10.1016/j.gca.2007.04.019, 2007.

Kirby, M. X., Soniat, T. M., and Spero, H. J.: Stable isotope sclerochronology of Pleistocene and Recent oyster shells (Crassostrea virginica), PALAIOS, 13, 560-569, https://doi.org/10.2307/3515347, 1998.

Kirkels, F. M. S. A.: Compilation of stable water isotopes in Indian Rivers, https://doi.org/10.1594/PANGAEA.912582, 2020.

Lear, C. H., Rosenthal, Y., Coxall, H. K., and Wilson, P. A.: Late Eocene to early Miocene ice sheet dynamics and the global carbon cycle, Paleoceanography, 19, https://doi.org/10.1029/2004PA001039, 2004.

LeGrande, A. N. and Schmidt, G. A.: Global gridded data set of the oxygen isotopic composition in seawater, Geophysical Research Letters, 33, 2006GL026011, https://doi.org/10.1029/2006GL026011, 2006.

Licht, A., van Cappelle, M., Abels, H. A., Ladant, J.-B., Trabucho-Alexandre, J., France-Lanord, C., Donnadieu, Y., Vandenberghe, J., Rigaudier, T., Lécuyer, C., Terry, D., Adriaens, R., Boura, A., Guo, Z., Naing Soe, A., Quade, J., Dupont-

Nivet, G., and Jaeger, J.-J.: Asian monsoons in a late Eocene greenhouse world, Nature, 513, 501-506, https://doi.org/10.1038/nature13704, 2014.

Lin, J., Liu, Y., Yang, Y., and Hu, Z.: Calibration and correction of LA-ICP-MS and LA-MC-ICP-MS analyses for element contents and isotopic ratios, Solid Earth Sciences, 1, 5-27, https://doi.org/10.1016/j.sesci.2016.04.002, 2016.

Liu, Y., Xu, J., Wang, Y., and Yang, S.: Trace metal bioaccumulation in oysters (Crassostrea gigas) from Liaodong Bay (Bohai Sea, China), Environ Sci Pollut Res, 28, 20682-20689, https://doi.org/10.1007/s11356-020-11968-6, 2021.

Ma, Y., Fan, M., Zhang, C., Grasby, S. E., Yin, R., Lu, Y., Zhang, B., Jin, X., Ma, C., Lu, Y., and Sluijs, A.: Volcanic and orbitally forced carbon release during the Middle Eocene Climatic Optimum, Geology, 52, 813-818, https://doi.org/10.1130/G52435.1, 2024.

Mamede, R., Santos, A., Díaz, S., Ferreira da Silva, E., Patinha, C., Calado, R., and Ricardo, F.: Elemental fingerprints of bivalve shells (*Ruditapes decussatus* and *R. philippinarum*) as natural tags to confirm their geographic origin and expose fraudulent trade practices, Food Control, 135, 108785, https://doi.org/10.1016/j.foodcont.2021.108785, 2022.

Martín-Martín, M., Tosquella, J., Guerrera, F., Maaté, A., and Martín-Algarra, A.: The Eocene carbonate platforms of the westernmost Tethys: a review, International Geology Review, 67, 573-605, https://doi.org/10.1080/00206814.2024.2397804, 2025.

McConnell, M. C., Thunell, R. C., Lorenzoni, L., Astor, Y., Wright, J. D., and Fairbanks, R.: Seasonal variability in the salinity and oxygen isotopic composition of seawater from the Cariaco Basin, Venezuela: Implications for paleosalinity reconstructions, Geochemistry, Geophysics, Geosystems, 10, https://doi.org/10.1029/2008GC002035, 2009.

Mezger, E. M., de Nooijer, L. J., Boer, W., Brummer, G. J. A., and Reichart, G. J.: Salinity controls on Na incorporation in Red Sea planktonic foraminifera, Paleoceanography, 31, 1562-1582, https://doi.org/10.1002/2016PA003052, 2016.

Miller, K. G., Browning, J. V., Schmelz, W. J., Kopp, R. E., Mountain, G. S., and Wright, J. D.: Cenozoic sea-level and cryospheric evolution from deep-sea geochemical and continental margin records, Science Advances, 6, eaaz1346, https://doi.org/10.1126/sciadv.aaz1346, 2020.

Miloikovitch, T.: Python Script and Dataset for Principal Component Analysis (Geosciences application), , https://doi.org/10.5281/zenodo.14776445, 2024.

Mitra, A. and Halder, K.: Tectonic and eustatic controls on the palaeobiogeographic distribution of Eocene bivalves, J Molluscan Stud, 90, eyae049, https://doi.org/10.1093/mollus/eyae049, 2024.

Mitra, A., de Winter, N. J., Miloikovitch, T., Halder, K., Ledésert, B. A., Claeys, P., and Müller, I. A.: Habitat Specific Growth Rate Adaptation in Oysters During Early Bartonian: Effects of High Temperature and Low Seasonality in the Indian Palaeotropics, Paleoceanography and Paleoclimatology, 40, e2025PA005129, https://doi.org/10.1029/2025PA005129, 2025.

Mitra, A., Dutta, R., and Halder, K.: A study on benthic molluscs and stable isotopes from Kutch, western India reveals early Eocene hyperthermals and pronounced transgression during ETM2 and H2 events, Swiss J Palaeontol, 141, 13, https://doi.org/10.1186/s13358-022-00255-1, 2022.

Moneer, E. S. M., Bazeen, Y. S., El-Sheikh, I., and Samir, A.: Taxonomic review, palaeoecological, and palaeobiogeographical significances of Campanian Tethyan oysters from the North Eastern Desert, Egypt, Sci Rep, 14, 13518, https://doi.org/10.1038/s41598-024-63379-z, 2024.

Montheil, L., Licht, A., Beard, K. C., Métais, G., Coster, P., Vaes, B., Donnadieu, Y., Pineau, E., Husson, L., and Dupont-Nivet, G.: Across ancient oceans: Eocene dispersal routes of Asian terrestrial mammals to Europe, Afro-Arabia and South America, Earth-Science Reviews, 273, 105352, https://doi.org/10.1016/j.earscirev.2025.105352, 2026.

Mouchi, V., Andrus, C. F. T., Checa, A. G., Elliot, M., Griesshaber, E., Hausmann, N., Huyghe, D., Lartaud, F., Peharda, M., and de Winter, N. J.: Oyster shells as archives of present and past environmental variability and life history traits: A multidisciplinary review of sclerochronology methods and applications, Limnology and Oceanography Letters, 10, 179-199, https://doi.org/10.1002/lol2.10461, 2025.

Mouchi, V., de Rafélis, M., Lartaud, F., Fialin, M., and Verrecchia, E.: Chemical labelling of oyster shells used for time-calibrated high-resolution Mg/Ca ratios: A tool for estimation of past seasonal temperature variations, Palaeogeography, Palaeoclimatology, Palaeoecology, 373, 66-74, https://doi.org/10.1016/j.palaeo.2012.05.023, 2013.

Mouchi, V., Godbillot, C., Forest, V., Ulianov, A., Lartaud, F., de Rafélis, M., Emmanuel, L., and Verrecchia, E. P.: Rare earth elements in oyster shells: provenance discrimination and potential vital effects, Biogeosciences, 17, 2205-2217, https://doi.org/10.5194/bg-17-2205-2020, 2020.

Mutti, M. and Hallock, P.: Carbonate systems along nutrient and temperature gradients: some sedimentological and geochemical constraints, Int J Earth Sci (Geol Rundsch), 92, 465-475, https://doi.org/10.1007/s00531-003-0350-y, 2003.

Nothdurft, L. D., Webb, G. E., and Kamber, B. S.: Rare earth element geochemistry of Late Devonian reefal carbonates, Canning Basin, Western Australia: confirmation of a seawater REE proxy in ancient limestones, Geochimica et Cosmochimica Acta, 68, 263-283, https://doi.org/10.1016/S0016-7037(03)00422-8, 2004.

Poitevin, P., Chauvaud, L., Pécheyran, C., Lazure, P., Jolivet, A., and Thébault, J.: Does trace element composition of bivalve shells record ultra-high frequency environmental variations?, Marine Environmental Research, 158, 104943, https://doi.org/10.1016/j.marenvres.2020.104943, 2020.

Piwoni-Piórewicz, A., Kukliński, P., Strekopytov, S., Humphreys-Williams, E., Najorka, J., and Iglikowska, A.: Size effect on the mineralogy and chemistry of Mytilus trossulus shells from the southern Baltic Sea: implications for environmental monitoring, Environ Monit Assess, 189, 197, https://doi.org/10.1007/s10661-017-5901-y, 2017.

Prasad, T. G. and Bahulayan, N.: Mixed layer depth and thermocline climatology of the Arabian Sea and western equatorial Indian Ocean. Indian journal of marine sciences, 25, 189-194, 1996.

Putten, E. V., Dehairs, F., Keppens, E., and Baeyens, W.: High resolution distribution of trace elements in the calcite shell layer of modern *mytilus edulis*: environmental and biological controls, Geochimica et Cosmochimica Acta, 64, 997-1011, https://doi.org/10.1016/S0016-7037(99)00380-4, 2000.

Racey, A.: A review of Eocene nummulite accumulations: structure, formation and reservoir potential. Journal of Petroleum Geology, 24 (1), 79-100, 2001.

Rai, S. P., Purushothaman, P., Kumar, B., Jacob, N., and Rawat, Y. S.: Stable isotopic composition of precipitation in the River Bhagirathi Basin and identification of source vapour, Environ Earth Sci, 71, 4835-4847, https://doi.org/10.1007/s12665-013-2875-0, 2014.

Ricardo, F., Pimentel, T., Génio, L., and Calado, R.: Spatio-temporal variability of trace elements fingerprints in cockle (Cerastoderma edule) shells and its relevance for tracing geographic origin, Sci Rep, 7, 3475, https://doi.org/10.1038/s41598-017-03381-w, 2017.

Rucker J. B., and Valentine J. W.: Salinity response of trace elements concentration in Crassostrea virginica. Nature 190, 1099-1100, 1961.

Saraswati, P. K., Khanolkar, S., Raju, D. S. N., and Banerjee, S.: An updated Eocene stratigraphy of Kutch. Geol. Soc. India Spec. Publ, 6, 25-31, 2016.

Saraswati, P. K., Khanolkar, S., and Banerjee, S.: Paleogene stratigraphy of Kutch, India: an update about progress in foraminiferal biostratigraphy, Geodinamica Acta, 30, 100-118, https://doi.org/10.1080/09853111.2017.1408263, 2018.

Sarkar, A., Sarangi, S., Ebihara, M., Bhattacharya, S. K., and Ray, A. K.: Carbonate geochemistry across the Eocene/Oligocene boundary of Kutch, western India: implications to oceanic O2-poor condition and foraminiferal extinction. Chemical Geology, 201, 281-293, https://doi.org/10.1016/S0009-2541(03)00238-9, 2003.

Sarr, A.-C., Donnadieu, Y., Bolton, C. T., Ladant, J.-B., Licht, A., Fluteau, F., Laugié, M., Tardif, D., and Dupont-Nivet, G.: Neogene South Asian monsoon rainfall and wind histories diverged due to topographic effects, Nat. Geosci., 15, 314-319, https://doi.org/10.1038/s41561-022-00919-0, 2022.

Schmidt, G. A., Bigg, G. R., and Rohling, E. J.: Global Seawater Oxygen-18 Database, v1.22, https://data.giss.nasa.gov/o18data/, 1999

Scholz, S. R., Petersen, S. V., and Anderson, B. M.: Modern reconstructions of mean and seasonal-scale climate from coastal marine gastropods (Turritellidae), Palaeogeography, Palaeoclimatology, Palaeoecology, 655, 112553, https://doi.org/10.1016/j.palaeo.2024.112553, 2024.

Schöne, B. R., Zhang, Z., Jacob, D., Gillikin, D. P., Tütken, T., Garbe-Schönberg, D., Mcconnaughey, T., and Soldati, A.: Effect of organic matrices on the determination of the trace element chemistry (Mg, Sr, Mg/Ca, Sr/Ca) of aragonitic bivalve shells (Arctica islandica)—Comparison of ICP-OES and LA-ICP-MS data, Geochemical Journal, 44, 23-37, https://doi.org/10.2343/geochemj.1.0045, 2010.

Sengupta, S., Parekh, A., Chakraborty, S., Ravi Kumar, K., and Bose, T.: Vertical variation of oxygen isotope in Bay of Bengal and its relationships with water masses, Journal of Geophysical Research: Oceans, 118, 6411-6424, https://doi.org/10.1002/2013JC008973, 2013.

Singh, A., Jani, R. A., and Ramesh, R.: Spatiotemporal variations of the δ18O-salinity relation in the northern Indian Ocean, Deep Sea Research Part I: Oceanographic Research Papers, 57, 1422-1431, https://doi.org/10.1016/j.dsr.2010.08.002, 2010.

Srivastava, V. K. and Singh, B. P.: Depositional environments and sources for the middle Eocene Fulra Limestone Formation, Kachchh Basin, western India: Evidences from facies analysis, mineralogy, and geochemistry, Geological Journal, 54, 62-82, https://doi.org/10.1002/gj.3154, 2019.

Stenzel, H. B.: Oysters. Treatise on Invertebrate Paleontology, Part N, Bivalvia 3, N953-N1224, 1971.

Steuber, T.: Isotopic and chemical intra-shell variations in low-Mg calcite of rudist bivalves (Mollusca-Hippuritacea): disequilibrium fractionations and late Cretaceous seasonality. International Journal of Earth Sciences, 88, 551-570, 1999.

Su, T., Feng, T., and Feng, G.: Evaporation variability under climate warming in five reanalyses and its association with pan evaporation over China, JGR Atmospheres, 120, 8080-8098, https://doi.org/10.1002/2014JD023040, 2015.

Surge, D. and Lohmann, K. C.: Evaluating Mg/Ca ratios as a temperature proxy in the estuarine oyster, Crassostrea virginica, Journal of Geophysical Research: Biogeosciences, 113, undefined-undefined, https://doi.org/10.1029/2007JG000623, 2008.

Tada, R., Zheng, H., and Clift, P. D.: Evolution and variability of the Asian monsoon and its potential linkage with uplift of the Himalaya and Tibetan Plateau, Progress in Earth and Planetary Science, 3, 4, https://doi.org/10.1186/s40645-016-0080-y, 2016.

Tardif, D., Fluteau, F., Donnadieu, Y., Le Hir, G., Ladant, J.-B., Sepulchre, P., Licht, A., Poblete, F., Dupont-Nivet, G.: The origin of Asian monsoons: a modelling perspective. Climate of the Past, 16, 847-865, https://doi.org/10.5194/cp-16-847-2020, 2020.

Tardif, D., Sarr, A.-C., Fluteau, F., Licht, A., Kaya, M., Ladant, J.-B., Meijer, N., Donnadieu, Y., Dupont-Nivet, G., Bolton, C. T., Le Hir, G., Pillot, Q., Poblete, F., Sepulchre, P., Toumoulin, A., and Banfield, W.: The role of paleogeography in Asian monsoon evolution: a review and new insights from climate modelling, Earth-Science Reviews, 243, 104464, https://doi.org/10.1016/j.earscirev.2023.104464, 2023.

Toumoulin, A., Tardif, D., Donnadieu, Y., Licht, A., Ladant, J.-B., Kunzmann, L., and Dupont-Nivet, G.: Evolution of continental temperature seasonality from the Eocene greenhouse to the Oligocene icehouse -a model-data comparison, Climate of the Past, 18, 341-362, https://doi.org/10.5194/cp-18-341-2022, 2022.

The Cenozoic CO2 Proxy Integration Project (CenCO2PIP) Consortium: Toward a Cenozoic history of atmospheric CO2, Science, 382, eadi5177, https://doi.org/10.1126/science.adi5177, 2023.

Tripati, A. K., Sahany, S., Pittman, D., Eagle, R. A., Neelin, J. D., Mitchell, J. L., Beaufort, L.: Modern and glacial tropical snowlines controlled by sea surface temperature and atmospheric mixing. Nature Geoscience, 7, 205-209, https://doi.org/10.1038/ngeo2082, 2014.

Tynan, S., Opdyke, B. N., Walczak, M., Eggins, S., and Dutton, A.: Assessment of Mg/Ca in *Saccostrea glomerata* (the Sydney rock oyster) shell as a potential temperature record, Palaeogeography, Palaeoclimatology, Palaeoecology, 484, 79-88, https://doi.org/10.1016/j.palaeo.2016.08.009, 2017.

Valdés-Vilchis, S., Sánchez-Beristain, F., Bernal, J. P., and Juárez-Aguilar, E. A.: Rare Earth Elements and Yttrium (REE+Y) patterns in recent *Anadara brasiliana* shells from Playa Norte, Barra de Cazones (Veracruz, Mexico): Evidence of anthropogenic contamination linked to river output?, Journal of South American Earth Sciences, 110, 103368, https://doi.org/10.1016/j.jsames.2021.103368, 2021.

Van Hinsbergen, D. J. J. van, Groot, L. V. de, Schaik, S. J. van, Spakman, W., Bijl, P. K., Sluijs, A., Langereis, C. G., and Brinkhuis, H.: A Paleolatitude Calculator for Paleoclimate Studies, PLOS ONE, 10, e0126946, https://doi.org/10.1371/journal.pone.0126946, 2015.

Verdin, A., Funk, C., Peterson, P., Landsfeld, M., Tuholske, C., and Grace, K.: Development and validation of the CHIRTS-daily quasi-global high-resolution daily temperature data set, Sci Data, 7, 303, https://doi.org/10.1038/s41597-020-00643-7, 2020.

Vialov, O.: Sur la classification des huîtres. *Comptes Rendus (Doklady) de l'Académie des Sciences de l'URSS.* ser. 2, 4, 17-20, 1936.

Wadood, B., Khan ,S., Khan ,A., Khan ,M. W., Liu ,Y., Li ,H., Ahmad ,S., and and Khan, A.: Diachroneity in the closure of the eastern Tethys Seaway: evidence from the cessation of marine sedimentation in northern Pakistan, Australian Journal of Earth Sciences, 68, 410-420, https://doi.org/10.1080/08120099.2020.1782472, 2021.

Westerweel, J., Roperch, P., Win, Z., and Dupont-Nivet, G.: Northward drift of the Burma Terrane with India during the Cenozoic and implications for the India–Asia collision, Geological Society, London, Special Publications, 549, 11–54, https://doi.org/10.1144/SP549-2024-18, 2025.

Xiao, W., Xu, Y., Zhang, C., Lin, J., Wu, W., Lü, X., Tan, J., Zhang, X., Zheng, F., Song, X., Zhu, Y., Yang, Y., Zhang, H., Wenzhöfer, F., Rowden, A. A., and Glud, R. N.: Disentangling Effects of Sea Surface Temperature and Water Depth on Hydroxylated Isoprenoid GDGTs: Insights From the Hadal Zone and Global Sediments, Geophysical Research Letters, 50, e2023GL103109, https://doi.org/10.1029/2023GL103109, 2023.

Zhang, F. and Emanuel, K.: On the Role of Surface Fluxes and WISHE in Tropical Cyclone Intensification, Journal of the Atmospheric Sciences, 73, 2011-2019, https://doi.org/10.1175/JAS-D-16-0011.1, 2016.